



**SPECTRAL ANALYSIS AND METASTABLE
ABSORPTION MEASUREMENTS OF HIGH
PRESSURE CAPACITIVELY AND
INDUCTIVELY COUPLED
RADIO-FREQUENCY ARGON-HELIUM
DISCHARGES**

THESIS

Ben Eshel

AFIT-ENP-13-J-02

**DEPARTMENT OF THE AIR FORCE
AIR UNIVERSITY**

AIR FORCE INSTITUTE OF TECHNOLOGY

Wright-Patterson Air Force Base, Ohio

DISTRIBUTION STATEMENT A
APPROVED FOR PUBLIC RELEASE; DISTRIBUTION UNLIMITED.

The views expressed in this thesis are those of the author and do not reflect the official policy or position of the United States Air Force, Department of Defense, or the United States Government. This material is declared a work of the U.S. Government and is not subject to copyright protection in the United States.

AFIT-ENP-13-J-02

SPECTRAL ANALYSIS AND METASTABLE ABSORPTION MEASUREMENTS
OF HIGH PRESSURE CAPACITIVELY AND INDUCTIVELY COUPLED
RADIO-FREQUENCY ARGON-HELIUM DISCHARGES

THESIS

Presented to the Faculty
Department of Engineering Physics
Graduate School of Engineering and Management
Air Force Institute of Technology
Air University
Air Education and Training Command
in Partial Fulfillment of the Requirements for the
Degree of Master of Science in Applied Physics

Ben Eshel, BA

June 2013

DISTRIBUTION STATEMENT A
APPROVED FOR PUBLIC RELEASE; DISTRIBUTION UNLIMITED.

AFIT-ENP-13-J-02

SPECTRAL ANALYSIS AND METASTABLE ABSORPTION MEASUREMENTS
OF HIGH PRESSURE CAPACITIVELY AND INDUCTIVELY COUPLED
RADIO-FREQUENCY ARGON-HELIUM DISCHARGES

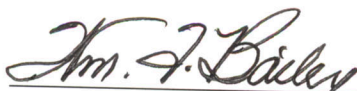
Ben Eshel, BA

Approved:



Dr. Glen P. Perram (Chairman)

29 May 2013
Date



Dr. William F. Bailey (Member)

29 May 2013
Date



Dr. Greg A. Pitz (Member)

17 May 2013
Date

Abstract

Characterization of the excited state argon population in an argon-helium discharge is of crucial importance to the development of a continuous wave Discharge Assisted Noble Gas Laser (DANGL). Experiments were conducted in the Richard W. Davis Advanced Laser Facility (DALF) at AFRL/RDLTD on Kirtland Air Force Base, Albuquerque, NM. During these tests the capability to maintain a capacitively coupled and inductively coupled radio-frequency discharge at pressures of 300 Torr was demonstrated. Optical Emission Spectroscopy (OES) experiments were conducted in order to examine the population distribution of the p-state in argon. The population distributions for these high-pressure and high-power cases were compared to a low-pressure, low-power pure argon discharge to examine the influence of helium on an argon discharge. Tuneable Diode Laser Absorption Spectroscopy (TDLAS) experiments were also performed on the inductively coupled discharge to examine the column density of the s5 and s3 metastable states for different discharge parameters. The absorption data was fit to an approximated Voigt profile from which pressure broadening rates of 18 ± 5.8 MHz/Torr and 22 ± 1.2 MHz/Torr were calculated for the 801.48 nm $p8 \rightarrow s5$ and 794.82 nm $p4 \rightarrow s3$ transitions, respectively.

Acknowledgements

I would like to take a moment to thank the people who made this project possible. I'd like to thank Dr. Glen Perram whose guidance and support made this work possible, Dr. Greg Pitz for providing us the use of his labs and equipment at AFRL/RDLTD and supporting the work with his insight, Mr. Donald Stalnaker for assisting us with the RF equipment in the labs and providing us with his expertise in the area of gas discharges, Mr. Ryan Richards for all his help during our two trips to AFRL/RDLTD to conduct this research, and finally, my family for always believing that I could climb any obstacle no matter how insurmountable it may have seemed to me.

Ben Eshel

Table of Contents

	Page
Abstract	iv
Acknowledgements	v
List of Figures	viii
List of Tables	x
I. Introduction	1
1.1 Motivation	1
1.2 Research Objective	2
II. Background	4
Chapter Overview	4
2.1 Current Research	4
2.2 Atomic Spectroscopy	5
Atomic Lineshape and Absorption Cross-section	5
Optical Emission Spectroscopy	7
Tunable Diode Laser Absorption Spectroscopy	8
Flow Rates	9
2.3 Argon Kinetics	10
Racah and Paschen Notation	10
III. Experimental Apparatus	13
3.1 Chapter Overview	13
3.2 CC RF Discharge	13
3.3 IC RF Discharge	13
3.4 CC OES Apparatus	14
3.5 CC and IC OES Apparatus	16
3.6 TDLAS Apparatus	17
IV. Radio-Frequency Gas Discharge Behavior	19
Chapter Overview	19
4.1 Capacitively Coupled Radio-Frequency Discharge	19
Passivation	19
Temperature Regulation	20
Pressure and Gas Mixture Impact on Performance	21
4.2 Inductively Coupled Radio-Frequency Discharge	25
Passivation	25

Temperature Regulation	26
Pressure and Gas Mixture Impact on Performance	26
4.3 Suggestions for Improvement	28
V. Results and Analysis	30
Chapter Overview	30
5.1 Test Matrix	30
5.2 Wavelength Calibration	30
5.3 Blackbody Calibration	33
5.4 Fluorescence Spectra	34
5.5 Population Distribution	41
5.6 Absorption Spectra	46
VI. Conclusions and Future Work	58
6.1 Future Work	59
Comparison of CC and IC metastable density trends	59
Discharge Engineering Design	60
Discharge and Gas Kinetic Model	61
Appendix A. Grotrian Diagram	63
Appendix B. Matching Network	64
Appendix C. IC and CC Spectra	66
Appendix D. Population Distributions	69
Bibliography	72
Vita	74

List of Figures

Figure		Page
1	Grotrian diagram of argon	11
2	Capacitively coupled RF discharge apparatus	14
3	Inductively coupled RF discharge apparatus	15
4	OES apparatus	15
5	TDLAS Apparatus.....	17
6	Capacitively coupled discharge at low pressure	22
7	Capacitively coupled discharge at high pressure	23
8	Inductively coupled discharge at high pressure and high power	27
9	Improved discharge cell design with water jacket	29
10	InGaAs blackbody spectrum and detectivity.....	35
11	ICCD blackbody spectrum and detectivity	35
12	Assigned argon spectra	36
13	CC spectra comparing various pressures and powers	38
14	Argon discharge spectra comparison	39
15	Excited state population distribution	42
16	CC population distribution comparing various pressures and powers	44
17	Electronic temperature trends as a function of pressure for multiple gas mixtures	45
18	Comparison of population distributions of IC and CC argon helium discharge with pure argon discharge	47
19	Voigt fits for the 801.48 nm p8 \rightarrow s5 transition absorption.	49

20	Voigt fits for the 794.82 nm p4 \rightarrow s2 transition absorption.	50
21	Lorentizan width as a function of pressure	51
22	Doppler width as a function of power	52
23	Comparison of absorbance and column density as a function of pressure for the s5 state	54
24	Comparison of absorbance and column density as a function of pressure for the s3 state	54
25	Comparison of absorbance and column density as a function of power for the s5 state	56
26	Comparison of absorbance and column density as a function of power for the s3 state	56
27	Grotrian diagram of argon with only s and p states.....	63
28	Modified Pi matching network diagram	64
29	CC discharge spectra for 5% argon at 100 Torr with powers ranging from 100 to 300 Watts	67
30	IC discharge spectra for 5% argon at 100 Torr with powers ranging from 600 to 800 Watts	68
31	CC discharge population distributions for 5% argon at 100 Torr with powers ranging from 100 to 300 Watts	70
32	IC discharge population distributions for 5% argon at 100 Torr with powers ranging from 600 to 800 Watts	71

List of Tables

Table		Page
1	CC OES test matrix	31
2	CC and IC OES test matrix.....	31
3	IC TDLAS Test Matrix.....	32
4	Spectral line intensity and transition comparison	40
5	Pressure Broadening Rates for the s5 metastable state	51
6	Pressure Broadening Rates for the s3 metastable state	52

SPECTRAL ANALYSIS AND METASTABLE ABSORPTION MEASUREMENTS OF HIGH PRESSURE CAPACITIVELY AND INDUCTIVELY COUPLED RADIO-FREQUENCY ARGON-HELIUM DISCHARGES

I. Introduction

1.1 Motivation

The United States Air Force has had an interest in high energy lasers for use in both strategic and tactical applications since the first kilowatt class chemical lasers were developed the mid-1970s. In just over a decade these chemical lasers scaled to megawatt class and proved their potential for weapons applications in multiple tests. This began a rapid development of military chemical laser weapons systems; the Mid-Infrared Advanced Chemical Laser (MIRACL), a megawatt class Deuterium Fluoride laser developed by the US Navy and first operational in the early 1980s, the 100 kilowatt class CO_2 laser developed by the US Air Force for the Airborne Laser Lab (ABLL) in the early 1970s and then later replaced by the megawatt class Chemical Oxygen Iodine Laser (COIL) in the early 1980s (18). These chemical lasers tend to be bulky systems that use or produce harmful and dangerous chemicals. This made development of these lasers tend towards a strategic rather than tactical approach. In 2003, Dr. William F. Krupke introduced the NIR Diode Pumped Alkali Laser (DPAL) which was to become the new focus for high energy laser weapons systems (13). Since its inception, the DPAL has been shown to be a high-gain system with high quantum efficiency. The alkalis act as a light converter, absorbing the incoherent radiation from the diodes and converting it into coherent laser light. The

high gain of the DPAL provides the potential ability to create smaller laser systems than what was accessible with the chemical lasers. Scaling efforts for these systems have proceeded rapidly due to large DoD interest. This research extends outside the US with the Russians publishing the development of the first kilowatt class cesium based DPAL (6). Unfortunately for these high-gain alkali systems, working with alkali metals is difficult due to the reactivity of the metals. The alkali metals tend to react with the windows used in the gain cells and with the organic compounds used for spin-orbit relaxation. In December 2012, Dr. Michael Heaven at Emory University published a paper that showed that the excited states of the noble gases can be used to form an analogous laser system to the DPAL. Dr. Heaven's discharge configuration, however, uses an excimer cavity which is a high voltage pulsed discharge (11). A recent effort to develop a continuous wave (CW) Discharge Assisted Noble Gas Laser (DANGL) requires the ability to reach high pressure, in the hundreds of Torr, in a CW discharge. These pressures are required in order to have enough spin-orbit relaxation to maintain CW lasing without significant bottlenecking. There are many methods to creating these high pressure discharges from simple radio-frequency capacitively and inductively-coupled discharges to more complex narrow-gap dielectric barrier discharges and micro-discharge arrays.

1.2 Research Objective

The purpose of this research was to demonstrate the ability of a standard RF discharge, be it capacitively or inductively coupled, to be used as the gain medium for the DANGL. This effort included showing the capability to sustain capacitively and inductively-coupled discharges at pressures of 300 Torr and above at the DALF on Kirtland AFB in Albuquerque, NM. The main focus of the final tests was to show the ability of the capacitively coupled and inductively coupled discharges to lase in

a quasi-CW state by pumping them using a long pulse (~ 200 ns), high intensity Ti:Sapphire laser. This effort was unsuccessful, shifting the focus of the experiment to measuring the absorbance of the metastable states in the inductively-coupled discharge using TDLAS. The absorption measurements were done in order to ensure that there was enough production of metastables to sustain laser action. Finally, fitting of the absorption measurements provides a first estimate for the pressure broadening rates of the argon metastable states.

II. Background

Chapter Overview

This chapter consists of two sections, the first of which discusses the current state of research with respect to high pressure discharges, argon and helium plasma models, measurement of excited state argon quenching rates and studies done on the excited state populations in argon discharges. The second section introduces all the concepts used in the analysis conducted later in this thesis.

2.1 Current Research

Atmospheric pressure plasmas are used in a myriad of manufacturing applications. Because of this large interest, the physics of these plasmas and discharges has been extensively studied for a wide range of radio-frequencies and pressures [(15),(17),(22)]. In order to support the scientific development, a large number of numerical models have been developed that are either discharge models that attempt to describe the discharge behavior, modeling the actual performance, power-loading and voltage-current relationships of the discharge (1), or are collisional-radiative models which describe ionization kinetics as well as production and destruction of excited states of gases in the discharge. For the argon helium discharges of interest there are many collisional-radiative models with large rate packages that treat pure argon [(8), (14),(26)] or pure helium (7) but none that treat the kinetics of an argon-helium gas mixture. These collisional-radiative models also tend to require certain conditions such as low-pressure or cold plasmas, both outside of the regime of the discharges described in this thesis. A cold plasma is one for which the degree of ionization is very low. Experimental measurements of the rates used in the kinetics packages are of the utmost importance and so there is a large effort to do just that. Quenching rates for the

excited states of the noble gases, with a large number of collision partners, are of interest to the discharge community and so many of these rates have been measured [(19),(20),(23)].

In order to validate the models the ability to measure the population distribution of these excited states and their trending behavior is required. The spectroscopic technique of OES is used for just that [(5),(12)]. This method allows for a wide study of energy levels since the limiting factor is the sensitivity of the detector and modern detectors and methods do an exceptional job of measuring small signals. To measure the metastable or higher state populations more precisely another method, known as TDLAS, is commonly used. The use of a laser allows for a significant increase in sensitivity and resolution as well as providing the ability to measure the spatial distribution of these concentrations (2). High-resolution absorption spectra can be fit to Voigt line-shapes in order to extract pressure broadening rates as well as gas temperature.

2.2 Atomic Spectroscopy

Atomic Lineshape and Absorption Cross-section

Atomic transitions are characterized by a few main quantities: the line-shape, the absorption cross-section and the saturation intensity. In general, there are two main contributions to the lineshape of an atomic transition, the Lorentzian part, a homogeneous line-shape, and the Doppler part, an inhomogeneous line-shape. The Lorentzian line-shape is of the form

$$g_L(\nu - \nu_0) = \frac{\Delta\nu_L}{2\pi((\nu - \nu_0)^2 + (\frac{\Delta\nu_L}{2})^2)} \quad (1)$$

where $\Delta\nu_L = \Delta\nu_l + \Delta\nu_c$ is the FWHM and is a combination of the natural line-

width of the transition, $\Delta\nu_l = \frac{A_{ij}}{2\pi}$ where A_{ij} is the Einstein A Coefficient of the $|i\rangle \rightarrow |j\rangle$ transition, and the collisionally broadened line-width, $\Delta\nu_c = \frac{1}{\pi T_2}$, where T_2 is the mean time between collisions (24). The collisionally broadened line-width is often represented as the product Pb where P is the gas pressure, usually in Torr, and b is the pressure broadening rate, in MHz/Torr. The Gaussian line-shape is a Doppler-broadened line-shape resulting from the velocity distribution of the atoms in the medium. The Doppler-broadened line-shape is of the form

$$g_D(\nu - \nu_0) = \frac{2}{\Delta\nu_D} \sqrt{\frac{\ln(2)}{\pi}} e^{-4\ln(2)\left(\frac{\nu - \nu_0}{\Delta\nu_D}\right)^2} \quad (2)$$

where the Doppler line-width is defined by $\Delta\nu_D = 2\nu_0 \sqrt{\frac{2\ln(2)k_B T}{mc^2}}$ (24). In general, an atomic transition will be neither entirely Lorentzian nor completely Gaussian, rather a convolution of the two. This convolution of the two line-shapes has been named the Voigt profile and is defined as

$$g_V(\nu - \nu_0) = \int_{-\infty}^{\infty} g_D(\nu'_0 - \nu_0) g_L(\nu - \nu'_0) d\nu'_0 \quad (3)$$

Unfortunately, the nature of being a convolution makes using the Voigt line-shape complex and often difficult to work with. Other things may influence these lineshapes such as transit-time broadening, power broadening and most importantly hyperfine structure. The three naturally occurring isotopes of argon have no nuclear spin and so there is no hyperfine structure. For the argon-helium gas discharges there is likely an electron broadening of the atomic transitions, a large Stark broadening due to the large electric fields inside the discharge, and a possible Zeeman effect from the magnetic fields.

The absorption cross-section for the transition is defined by

$$\sigma(\nu_{ij}) = \frac{g_i}{g_j} \frac{A_{ij}}{8\pi} \lambda_{ij}^2 g(\nu) \quad (4)$$

The cross-section is often used at its line center value of $\sigma_{ij}(\nu_0)$ (24). The absorption cross-section combined with the lifetime of the upper-state is used to define the saturation intensity of a transition. This is the intensity at which the gain drops to half of the small-signal gain. The saturation intensity also defines the transition from an exponential increase in stimulated emission with a linear increase in pump intensity to the linear regime. The saturation intensity is defined as

$$I_{sat} = \frac{h\nu_{ij}}{\sigma_{ji}\tau_j} \quad (5)$$

where ν_{ij} is the frequency of the transition, σ_{ji} is the stimulated emission cross-section related to the absorption cross-section by $\sigma_{ij} = \frac{g_i}{g_j}\sigma_{ji}$, and τ_j is the lifetime of the upper state (24).

Optical Emission Spectroscopy

Optical Emission Spectroscopy (OES) is used to study the population distribution of excited atomic species. If the Einstein A Coefficients are known for the transition then an effective population can be derived from the spectral intensity. The total intensity of a line is proportional to the population in the upper state and the Einstein A coefficient, if only spontaneous emission is considered. That population is then proportional to the degeneracy of the upper state times the Boltzmann factor for the transition:

$$I_{ij} \propto A_j N_j \propto A_{ij} g_j e^{-\frac{\Delta E}{k_B T}} \quad (6)$$

where i denotes the lower state, j denotes the upper state, N_j is the population in the

upper state, A_{ij} is the Einstein A coefficient of the transition, g_j is the degeneracy of the upper state, ΔE is the energy of the transition, k_B is the Boltzmann constant and T is the gas temperature. This equation can be rewritten as the following relationship:

$$\ln\left(\frac{I}{A_j g_j}\right) \propto \frac{-\Delta E}{k_B T} \quad (7)$$

The term on the LHS is related to the population as defined above and so it is referred to as the effective population. If the system is in equilibrium then the LHS can be plotted against the RHS and it should fit on a line with slope $-\frac{1}{k_B T}$. While generally used to extract gas temperatures, this is the method can be used to derive a temperature from any Boltzmann distribution and is used in Chapter 5 to get an electronic temperature from the effective population.

Tunable Diode Laser Absorption Spectroscopy

Another method for studying the population of a certain excited state is Tunable Diode Laser Absorption Spectroscopy (TDLAS). This method uses a laser, with intensity much lower than the saturation intensity of the transition of interest, to scan over the absorption feature. By measuring the intensity before and after the medium an absorbance can be calculated. Then, if we know the absorption cross-section and path length we can use Beer's law of attenuation (24) to get the number density:

$$I = I_0 e^{-\sigma n l} \quad (8)$$

Solving this for the number density we get:

$$n = \frac{1}{\sigma l} A \quad (9)$$

where $A = -\ln\left(\frac{I}{I_0}\right)$ is the absorbance.

Flow Rates

The flow rate of the gas through the cell can be calculated using the incompressible Bernoulli equation as it relates to streamline flow. The pressure drop over an orifice is given by:

$$\Delta p = \frac{1}{2}\rho V_2^2 - \frac{1}{2}\rho V_1^2 \quad (10)$$

where ρ is the gas density and V is the flow velocity (4). We can convert this to a volumetric flow rate using the continuity equation which gives us:

$$\Delta p = \frac{1}{2}\rho Q^2 \frac{1}{A_2^2} \left[\left(1 - \frac{A_2}{A_1} \right)^2 \right] \quad (11)$$

where Q is the volumetric flow rate and A_1 , A_2 are the cross-sectional areas of the flow (4). Solving for the volumetric flow rate and substituting in the flow coefficient C_f and orifice area to account for the real flow conditions and the unknown area of the flow downstream we get the expression:

$$Q = C_f A_0 \sqrt{\frac{2\Delta p}{\rho}} \quad (12)$$

The velocity of the flow will be given simply by the ratio of the volumetric flow rate to the area of the flow tubes:

$$v = \frac{Q}{A} \quad (13)$$

2.3 Argon Kinetics

Racah and Paschen Notation

Angular momentum coupling schemes are used to describe and organize the energy level spacings of an atom. For most light atoms, where electrostatic effects dominate any magnetic interactions, Russell-Saunders or L-S coupling is used. In this scheme the orbital angular momenta of the electron, \vec{l} and their spins \vec{s} are combined separately. The two are then summed to give a total angular momentum, $\vec{L} + \vec{S} = \vec{J}$. For heavier atoms, where the dominant interaction is magnetic, the j-j coupling scheme is used. For this scheme the orbital angular momentum and spin of each individual electron are first summed, $\vec{s} + \vec{l} = \vec{j}$ and then these individual total angular momenta are added in order to get the total angular momentum, $\sum \vec{j}_i = \vec{J}$. The energy level of the excited noble gases are not well described by either j-j coupling or l-s coupling. An intermediate coupling scheme has been developed and is known as j-l coupling. The coupling scheme is referred to as Racah notation (9). This notation is of the form $nl(J_{core})[K]J$, where n is the electronic quantum number, l is the electron orbital angular momentum, J_{core} is the total angular momentum of the core represented by L-S coupling notation, K is the total angular momentum of the core coupled with the orbital angular momentum of the electron, $\vec{K} = j_{core} + \vec{l}_e$, and J is the total angular momentum given by $\vec{J} = \vec{K} + \vec{s}$. Paschen notation is also used for this complex energy level distribution. It is a simple notation that combines a letter, the letter associated with the orbital angular momentum, and a number that is unrelated to the energy and only an ordering.

The energy levels denoted with both Paschen and Racah notation for the s, p and d excited states is shown in Figure 1. Vertical lines represent the dipole allowed transitions. A version of the Grotrian diagram that focuses on the s and p states can be found in Appendix A.

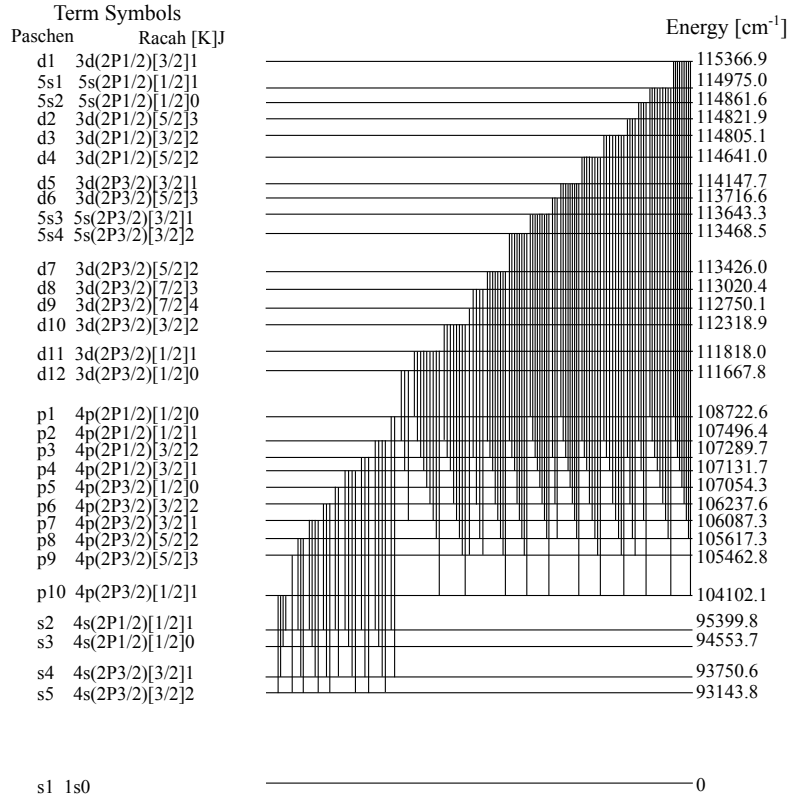


Figure 1. The energy level diagram for excited argon is shown. The levels are denoted both by their Paschen and Racah designations on the left as well as their distance from ground on the right.

Clearly, the energy level scheme for the noble gases is more complicated than that of the alkalis. This can be both a benefit and a drawback. The benefit is in the potential tunability of a laser system. There is the potential capability to construct both three and four level lasers in a myriad of different transitions. The drawback is in the complicated kinetics of the excited states in the discharge and the strong coupling between them. The laser performance may also be reduced due to the multi-photon and multi-electron ionization paths that arise from the proximity of ionization to these excited states.

III. Experimental Apparatus

3.1 Chapter Overview

Two separate experiments using three different sets of equipment and configurations and two discharge types were set up over two separate experiments at the DALF on Kirtland Air Force Base in Albuquerque, NM. The first was set up to conduct OES experiments on a high pressure capacitively-coupled radio-frequency discharge. The second, also an OES apparatus, and third, a TDLAS apparatus, were both set up during a laser demonstration test, also at the DALF. The two distinct discharge configurations are first introduced and are followed by an explanation of the experimental setups.

3.2 CC RF Discharge

The capacitively-coupled RF discharge cell consisted of an MDC Pyrex tube measuring 1" in length and 7/16" in diameter. The RF electrodes (HV, ground) were separated by 57.6 mm (2.27"). The effective discharge length is that of the cell since the plasma connects the HV to the ground by means of the Pyrex-Steel boundary. Air flowed over the tube using the 120 PSI building air source. A diagram of the cell is shown in Figure 2.

3.3 IC RF Discharge

The inductively-coupled radio-frequency discharge cell consisted of an MDC Double Ended 7052 Glass (Pyrex) - UHV Series tube measuring 67.9 cm (26.71"). A solenoid is coiled around the tube and insulated using a fibrous cloth. The solenoid has a diameter of 1.5" and contained 15 turns separated by 0.69 cm (0.27") over a

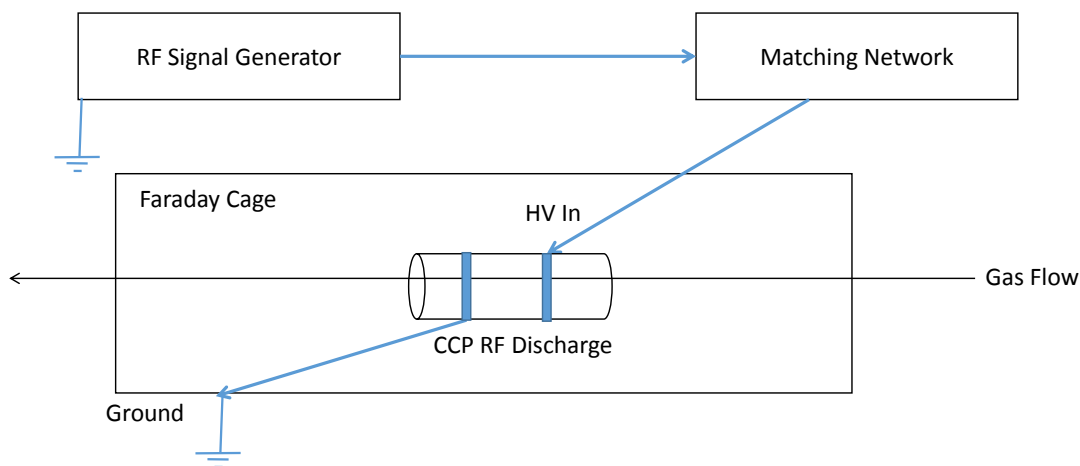


Figure 2. Shows the basic apparatus used to directly couple the RF source to the discharge cell. The diagram does not include the vacuum equipment or cooling flow.

total length of 20.07 cm (7.9"). Deionized water was flowed through the solenoid in order to keep the coils cool. A diagram of the cell is shown in Figure 3.

3.4 CC OES Apparatus

The fluorescence spectroscopy apparatus is shown in Figure 4.

The radio-frequency signal was generated by an ENI RF Generator, Model GHW-12A-13DF2NO. The RF generator is a water-cooled signal generator that produces RF power ranging from 1 - 1250 Watts at a set frequency of 13.56 MHz. It was wired to a custom designed matching network, the design details of which are left to Appendix B. The RF generator was directly connected to the CC cell. The cell was air cooled using the 120 PSI building airflow.

Fluorescence was collected from the end of the discharge cell through a window 1/2" in diameter. A trifurcated fiber with a collimating lens was placed 1/2" from the end of the cell. One section was coupled directly into a ARC SpectraPro 300i 0.3 meter triple grating monochromator set to 300 gr/mm with a 1.0 micron blaze.

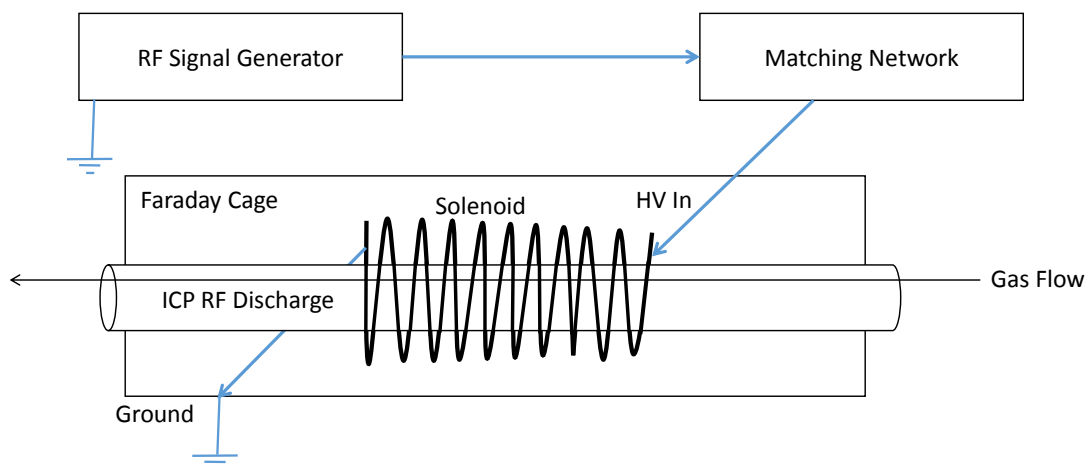


Figure 3. Shows the basic apparatus used to inductively couple the RF source to the discharge cell. The diagram does not include the vacuum equipment or cooling flow.

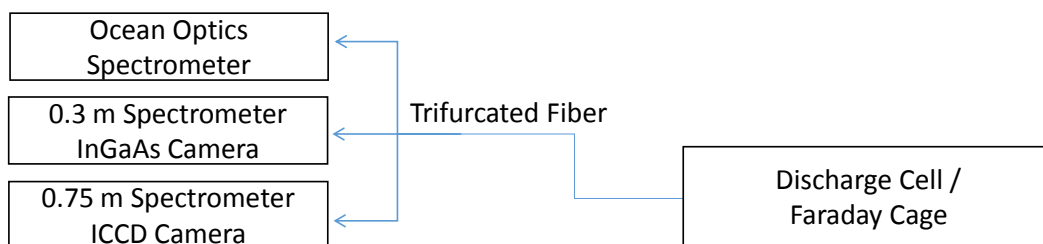


Figure 4. Shows the basic apparatus used to collect fluorescence of the discharge. Light emitted at the end of the cell enters a collimation optic on the fiber which is then coupled directly to the 0.3 meter and 0.75 meter monochromator with an InGaAs and ICCD detector, respectively, and the Ocean Optics spectrometer

The monochromator was connected to an Acton 7498-0001 InGaAs detector array of 1024x1. The detector response for the InGaAs is between 800 and 1600 nm. The second was coupled into a SpectraPro 2750 0.75 meter triple grating monochromator set to 600 gr/mm and a 1.0 micron blaze. It was connected to a Roper Scientific 7346-0001 Intensified CCD detector array of 1340x100. The detector response for the ICCD is between 500 and 950 nm. The third fiber was connected to an Ocean Optics spectrometer which was simply used to monitor the whole spectral range. This became useful when spectral lines appeared around 590 nm as the cell heated up.

Welding Grade Argon, with a 99.996% purity, flowed into a 500 PSI mixing tank along with Helium before entering the cell. This was done to allow a precise mixture of argon and helium to be made and flow consistently for long periods of time. The gas flowed from the mixing tank into a regulator that controls the pressure on a 0.01" orifice before flowing into the cell before the High-Voltage input and out after the electrical ground to vacuum. A needle valve at the end of the flow was used to control the gas pressure. Flow rates were calculated to be on the order of a few cm/s.

3.5 CC and IC OES Apparatus

The fluorescence spectroscopy apparatus is similar to that of the previous test. The same ICCD detector was used connected to the 0.75 m monochromator. Some minor changes were made from the previous fluorescence apparatus. The ENI RF generator was used for the CC spectra. For the IC spectra the RF signal generator was changed to a Macaroni Instruments 10 kHz - 1 GHz signal generator (2022C). The signal was fed into a Amplifier Research Model 3500A100 10 kHz - 100 MHz 3500 Watt RF signal amplifier. A TENMA spectrum analyzer was set up to track RF radiation in the room, of which there was a measurable amount.

For the changes in the fluorescence collection the InGaAs detector was removed.

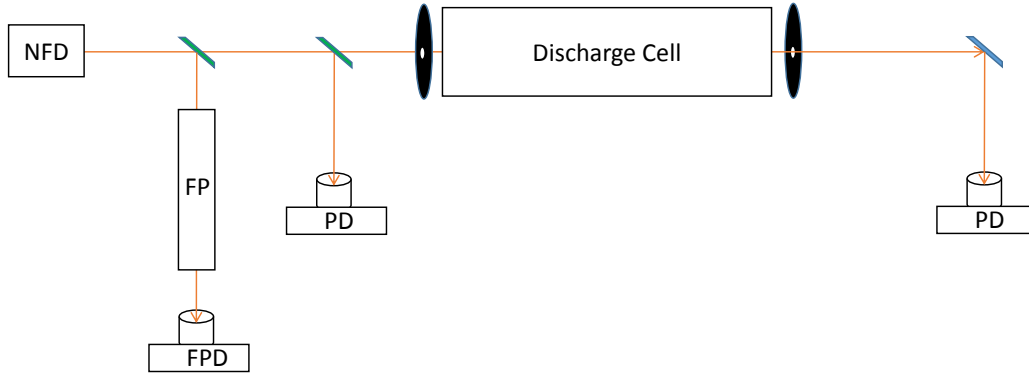


Figure 5. Shows the basic apparatus used to measure the input power and output power of a laser used to investigate the number density of metastable argon. The laser is split twice, the first of which goes through a Fabry-Perot etalon in order to calibrate a relative frequency axis. The second reflected piece goes to a photo-diode as the incident power. The beam that goes through the cell goes through a pinhole and is reflected to a photo-diode in order to minimize the fluorescence signal picked up by the photo-diode. The diagram does not include the vacuum equipment or cooling flow.

The grating in the SpectraPro 2750 0.75 meter monochromator was changed from 600 gr/mm and 1.0 micron blaze to 1200 gr/mm and a 500 nm blaze. This allowed for collection of higher resolution spectral data. The trifurcated fiber was replaced with a CeramOptec 9393 WF200/220P28 5.0 meter fiber with a Thor Labs LA1951-C 25.4 mm focus, planoconvex lens to focus the light into the fiber. The gases were switched out to Ultra-High Purity Argon (99.999% purity) and Ultra-High Purity Helium (99.999% purity).

3.6 TDLAS Apparatus

For the absorption tests the discharge cell was changed from a CC RF discharge to an IC RF discharge. The apparatus is shown in Figure 5.

The absorption measurements were done using a New Focus Diode Laser Model 6314 with a tunable wavelength range of 794 - 804 nm. The laser was controlled using a Velocity TLD-6300-LN Controller with the laser scanning controlled externally by a wavefunction generator.

The laser was sent through two Thor Labs EBP1 30:70 economy beam splitters and then through the center of the discharge cell. The first reflected piece of the laser was sent through a Coherent 33-6263-001 Fabry-Perot etalon with a 300 MHz FSR and was collected by a New Focus Model 1621 visible fast (1 ns rise time) photo-diode. The reflection from the second beam splitter was sent to a New Focus Model 2033 visible photo-diode. On the exit of the cell the laser was fed through a pinhole to block the discharge fluorescence and then reflected off of a Thor Labs EO3 broadband mirror to another New Focus Model 2033 visible photo-diode. The fast photo-diode was connected to a PSI Voltage Amplifier to compensate for the weak signal due to the low intensity exiting the etalon. The photo-diodes were connected to an Agilent Infiniium Vision DSO5034A Oscilloscope with a 300 MHz Response. The oscilloscope was connected to a computer to allow readouts at higher sampling rates, of 100,000 points per scan, than the oscilloscope alone, at a maximum of 1,000 points per scan. The RF radiation, mentioned previously, was large enough to impact the voltage measured on the fast photo-diode. This was only a mild problem, however, as the peaks of the etalon were still discernible for most test conditions.

IV. Radio-Frequency Gas Discharge Behavior

Chapter Overview

In this chapter the qualitative behavior of the low and high-pressure capacitively and inductively-coupled discharges is discussed. This discussion includes any cell passivation, temperature regulation and heating issues, and overall discharge performance in the large range of pressures and powers tested. The first section discusses these behaviors in a CC discharge. The second discusses the same for the IC discharge. The last section introduces some design improvements that could be made to improve performance.

4.1 Capacitively Coupled Radio-Frequency Discharge

The performance of the CC RF discharge, in the configuration described previously, is sensitive to a broad range of parameters. Of those parameters the most important are passivation, internal and external temperature, gas flow rate, gas pressure and Argon/Helium ratio. It is also worth noting that the RF interference generated by the CC discharge is significantly lower than that of the IC discharge. The RF radiated into the room tended to be so low that the Faraday cage could be left open without causing interference with electrical equipment.

Passivation

The cells used for the CC discharge undergo a level of passivation before discharges inside are stable. The discharge in the cell terminates on any defects on the inside of the cell, mainly near the Pyrex-steel boundary. These defects heat up locally and likely melt. This occurs because the electrodes are connected to the steel pipe which causes the steel itself to act as the RF source and ground. Passivation is

only important for the cells at high pressure when the discharge volume is greatly reduced and appears as a pillar rather than filling the whole cell. The location where the discharge pillar terminates on the ends of the cell is highly dependent on the passivity and will oscillate before passivation occurs. At low pressures, however, the discharge is stable in the cell and likely extends farther than what is visible inside the Pyrex cell. This implies that passivation is a result of the Pyrex-steel boundary being close to the discharge volume, offering a better electrical connection than any other surface. Passivation leads to inconsistent discharge behavior as the high pressure pillar will terminate on the boundary in the location that gets passivated first due to either its proximity to the RF source or because of material or manufacturing inconsistencies.

Temperature Regulation

The CC discharge suffers greatly in the area of temperature regulation. The RF electrodes must be directly cooled in order to prevent the steel from heating up to temperatures greater than 300 °C. Temperatures in this range quickly break the Pyrex due to the rapid heating and different expansion rates of the two materials. Unfortunately, external cooling appears to be insufficient even if one could keep the surface temperature well below 70 °C. Flow rate influences both the internal temperature of the plasma. The increase in flow rate will reduce the impact of heating from diffusion of the plasma to the Pyrex boundary. It also reduces the amount of time the gas spends inside the discharge, reducing its overall temperature. As mentioned previously, the discharge pillar connects with the Pyrex-steel boundary. The binding material has a relatively low melting point and will heat up sufficiently to disconnect the Pyrex from the steel tube. This limitation inhibits the ability to use the discharge at higher powers in order to produce a larger metastable population. At powers of

300 W and above, the cells only last for 3 - 5 minutes of continuous use before breaking. Powers greater than 500 Watts seem necessary to produce enough metastable population to build a laser for the capacitively-coupled system and so a solution to this internal heating issue will be required. At these higher powers an orange glow is clear and the Sodium D lines show up in the spectra.

Pressure and Gas Mixture Impact on Performance

At low pressure the CC discharge fluorescence fills the whole discharge cell and likely spreads beyond what is visible. This is because observable part of the fluorescence is from the Pyrex cell and any other fluorescence is obstructed by the steel pipe. The fluorescence brightness gives a qualitative measure of the excited state population. The discharge being completely illuminated implies a large excitation and a relatively homogeneous excitation in the cell. As power is increased for a fixed pressure the fluorescence intensity increases. For a pressure increase at a fixed power the fluorescence intensity decreased. Discharge length appears to be independent of pressure but this is likely only because the cell was so short that the discharge could terminate on the cell ends. An example of a low pressure discharge is shown in Figure 6.

As pressure is further increased not only does the discharge fluorescence decrease but the diameter also drops significantly. The final result is a barely illuminated cell with a bright discharge pillar between the steel ends. While the pillar is bright relative to the background it is much less so than the fully illuminated low pressure cell. The pillar is clearly seen in Figure 7.

The pillar becomes increasingly unstable and dims as pressure increases. As pressure continues to increase the discharge flickers as it continues to dim and will go out unless an increase in power is used to restore some stability and brightness. Power-

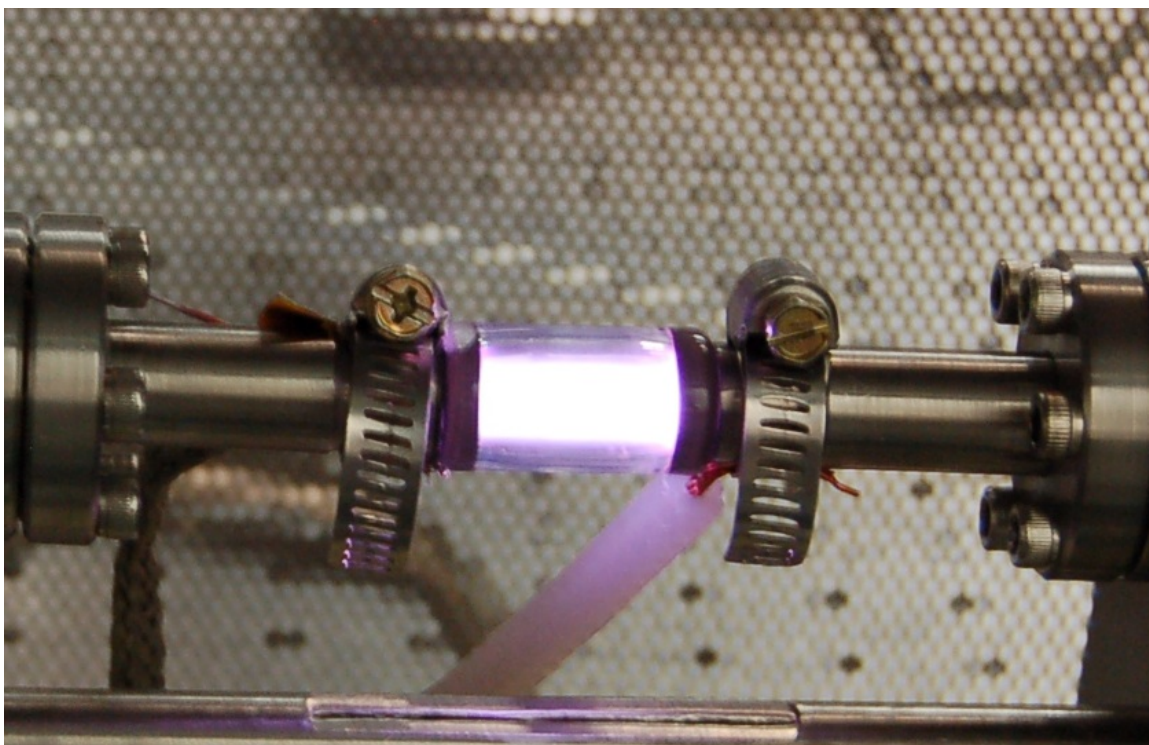


Figure 6. The capacitively coupled discharge is fully illuminated and glows a bright purple color. The color originates from the large number of transitions in the red part of the spectrum, from the first p-state to the first s-state, and the blue lines from the higher excited s-states to the first excited p-state. The ground and high voltage source are held by clamps on the left and right sides of the cell, respectively. The discharge conditions were an Ar/He mixture with 5% argon at 10 Torr and 100 Watts.

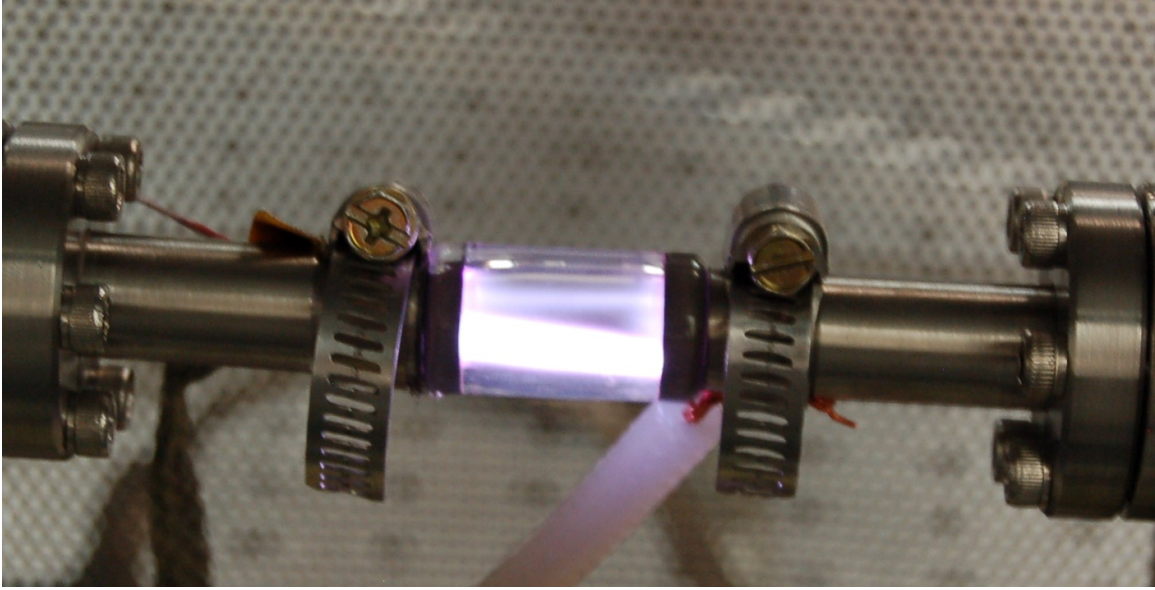


Figure 7. The discharge volume is partially illuminated and glows a bright purple color. The discharge pillar is clearly visible towards the bottom of the cell and curves to terminate near the RF source on the bottom right of the cell. The discharge pillar is also asymmetric, widening as it approaches the ground on the left. The discharge conditions were an Ar/He mixture with 5% argon at 100 Torr and 150 Watts.

loading is limited, however, by the internal heating it causes, as previously mentioned.

The last parameter that greatly impacts performance is the ratio of argon to helium in the gas mixture. From the low to high pressure tests conducted, performance of the mixtures is basically indistinguishable at low pressures (<50 Torr) but as pressure reaches 300 Torr the stability of the discharge varies widely for the various mixtures. As the percentage of argon in the gas mixture increases the discharge becomes continually more difficult to ignite at low pressures and collapses more rapidly as pressure increases. The main observation that distinguishes the cases is the color of the glow in the discharge. In general, helium glows a very light pink and argon glows a deep purple. These colors come from the energy level distribution of the atoms. The Grotrian diagram for the argon atoms for the first few states is shown but the full diagram would have energy levels that go to $30d$. There are a large number of intense transitions from these higher lying states to the $4p$ states studied in this

document. The purple glow comes from the combination of these blue lines with the large number of red and NIR lines that arises from the $4p \rightarrow 4s$ transitions and $3d \rightarrow 4p$ transitions. Helium in the discharge emits over the whole visible spectrum with a majority of the visible lines in the red and NIR. This creates the mostly white fluorescence with a pink tint. Most of the strong transitions in Helium are in the UV and in the NIR-FIR range and so do not impact the observed color of the fluorescence. Another trend that arises from increasing argon percentage is the discharge becoming increasingly difficult to ignite as the percentage of argon in the gas mixture increases. Also, high pressure performance changes with increasing argon percentage. That is, more argon in the gas mixture increases the instability of the discharge pillar at high pressures. The plasma becomes more sensitive to small changes in the aforementioned parameters. Often this instability reveals itself as an oscillation of the discharge pillar about the inside of the cell. These instabilities are likely thermally driven. The ionization level of argon is significantly ($70,000 \text{ cm}^{-1}$) lower than the ionization level of helium. At higher argon percentages we would expect the discharge performance, from the perspective of ionization, to increase. This is not what is observed as so thermal effects must be considered. The higher argon percentages mean lower helium percentages. Helium, being a light atom, is an effective thermal manager and increases the thermal conductivity of the plasma. Lower percentages of helium in the discharge should cause the plasma to run hotter. Unfortunately, the plasma temperature is not a quantity that was measured during these tests nor is it an easy quantity to measure with this apparatus. There is, however, a clear trade between thermal management of the plasmas in the discharge and the ionization percent. The last impact that a large percentage of argon has on the discharge has to do with the RF source itself. The RF signal generator is connected to a custom matching network as described in Chapter 3. For high percentages of argon the load changes more significantly with

pressure causing large increases in reverse power with moderate increases in pressure. Furthermore, as the discharge pillar oscillates in the cell the reverse power oscillates with the same frequency making load matching extremely difficult and allowing for heating in the components of the matching network. Finally, worth considering are the influence of the inner diameter (I.D.) of the cell on the stability of the discharge. Tests were repeated using a 9/16" I.D. cell and some notable changes were observed. For the larger I.D., the discharge fluorescence was visibly reduced. The discharge in the larger cell tended to run with a reduced heat load but suffered from the previously mentioned instabilities at lower pressures than the smaller I.D. cases.

4.2 Inductively Coupled Radio-Frequency Discharge

The performance of the IC RF discharge is sensitive to a narrower range of parameters when compared to the CC discharge. Performance is strongly dependent on internal temperature, gas pressure and argon/helium ratio. RF interference for the IC case is significantly greater than for the CC case. The solenoid is a much larger RF source than the simple antennae formed by the CC RF source on the cell. This makes the matching network significantly more important since a better matching of the source to the load reduces not only the reverse power fed into the RF signal generator but also minimizes the RF emitted into the room, thereby minimizing the electrical interference.

Passivation

As mentioned above, the IC discharge does not require passivation. This is because at higher pressures the IC discharge does not form a pillar that connects with the Pyrex-steel boundary and so the discharge is not dependent on the condition of that boundary. The lack of passivation allows for more consistent behavior and less

dependence on manufacturing.

Temperature Regulation

In contrast to the CC case, the IC case is significantly simpler to externally cool, or cool the RF source. The long cell configuration also removes the discharge termination effects on the Pyrex-steel boundary. Unfortunately, the need to run at significantly higher powers exacerbates the internal heating problem of the cell. The solenoid that is used to generate the discharge has deionized water flowing through the coils and so is cooled effectively, except for a small distance about the HV source. This only partially solves the external heating problem. In the configuration described in Chapter 3 the solenoid is resting on the tube. Even though it is insulated from the coil, the section of the tube closest to the RF source heats up significantly. This heating caused a distinct orange glow in the discharge. This orange glow is apparent in Figure 8 extending far beyond the HV source.

Over time this heating causes a softening of the Pyrex which causes it to warp under vacuum and gas flow leading to the divot seen in Figure 8.

Pressure and Gas Mixture Impact on Performance

The IC discharge at low pressures (<30 Torr) illuminates the full glass tube. Upstream of the discharge tends to glow a white/pink implying more Helium excitation and downstream tends towards a darker purple. Asymmetric performance is a potential problem in the IC discharge. As pressure increases the downstream glow shortens first until it reaches the solenoid. The insulation is opaque and so any changes in discharge length beyond that point were not visible but it is assumed that the discharge length continued to decrease until it reached a couple of centimeters left of the RF source. Through this change the full width of the cell remains illuminated. This



Figure 8. The discharge volume glows brightly along the whole cell but the bright orange Pyrex fluorescence overwhelms the weaker purple glow of the Argon/Helium discharge. A divot in the Pyrex is visible on the right side of the solenoid. This glow became common when working with the IC discharge at pressures above 200 Torr and powers above 800 Watts.

is in great contrast to the CC discharge in which the length remains a constant but the radius of the discharge decreases with increasing pressure. Increasing RF power restores discharge length and increases fluorescence in a similar manner to the CC case. During these increases in pressure the upstream fluorescence tends not to change brightness. Increasing pressure further, beyond the point where the downstream glow receded into the solenoid, leads to decreases in the fluorescence brightness and length of the upstream glow. This continues until the discharge is fluorescing a couple of centimeters around the RF source in a spherical shape. Unlike the CC case, no instabilities are seen when the discharge approaches the limit of remaining lit. The ratio of Argon to Helium in the gas mixture also has less impact than in the CC case. For high percentages of Argon, like the CC case, the discharge became increasingly difficult to ignite. Unlike the CC case, however, that is where the difficulty ends. The higher Argon percentage appears to have no impact on discharge performance beyond the initial difficulty. It is interesting to note that as Argon percentage increases the upstream fluorescence does take on a more purple tone. This is caused by a larger amount of upstream Argon being excited.

4.3 Suggestions for Improvement

Both the CC and IC configurations would be greatly improved by changing the cells currently used. Replacing this short cell, in the CC case, with a long Pyrex tube, as in the IC case, will help reduce both external and internal heating problems as well as remedying the inconsistencies caused by manufacturing. For both cases, a deionized water jacket should be placed on the cell provided the RF source is insulated properly. A diagram of this apparatus is given in Figure 9.

This water flow would provide quieter and more effective cooling of the cell in comparison to the air flow used previously. In the CC case this insulation is as simple as

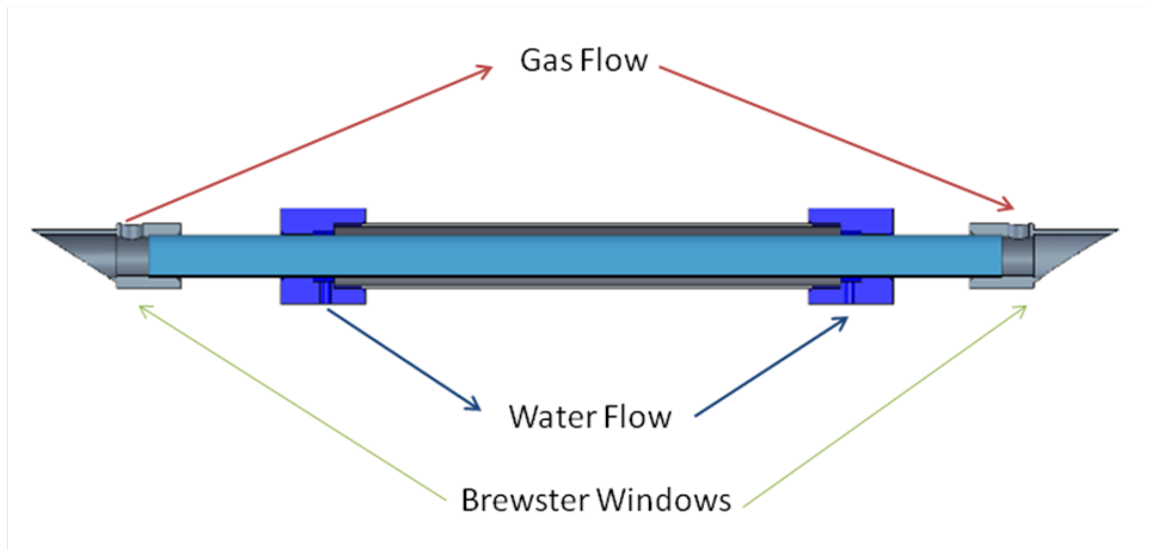


Figure 9. An improved discharge cell configuration has a water jacket around the discharge cell. Deionized water flows through this jacket and will cool the cell and prevent it from melting when the discharge is operating at high power.

providing a copper jacket for the RF source. In the IC case this becomes significantly trickier. A first step would be to study the heating of cell if the solenoid floats above the cell instead of resting directly on it. This simple change will likely minimize the heat loading issue allowing air cooling of the tube to be sufficient. If not, a more complex solution may be necessary, such as dielectric cooling of the whole system. A liquid nitrogen jacket is not recommended as Pyrex has a tendency to crack when subject to large thermal gradients, as it would be in this case. Reducing the I.D. of the cell will likely offer more stability as well since the parameter of interest in a discharge is the pressure diameter product and so lowering the diameter to 1/4" will allow a 175% increase in pressure without changing this product.

V. Results and Analysis

Chapter Overview

In this chapter, the data analysis conducted with the fluorescence spectra and absorption data is discussed. The first section shows the full test matrix for the two tests. The second and third sections explain the details of the wavelength and black-body calibration, respectively. The third section shows an example of the fluorescence spectra and compares the spectra for different discharge types. The fourth section discusses the population distributions derived from the spectra in the CC and IC discharges and their trending behavior. The fifth section discusses the collected absorption data and line-shape fits done to extract line-widths and pressure broadening rates.

5.1 Test Matrix

Data was collected for a significant number of different pressures, powers, gas mixtures and discharge configurations. For the first CC OES tests the main limitation was the heating problems associated with the RF which limited both peak RF power and the peak pressure. The full test matrix for the fluorescence spectroscopy is given by Table 1 and Table 2. The test matrix for the absorption spectroscopy experiment is given in Table 3

5.2 Wavelength Calibration

The data was broken into monochromator scans with separate wavelength centers. These scans overlapped by 40 nm for the four scans of the InGaAs over the range of 700 - 1600 nm and overlapped by 6 nm for the six scans of the ICCD over the range of 700 - 1000 nm.

Table 1. Capacitively-coupled OES test matrix

Argon Percentage	Pressure [Torr]	Power [Watts]	Cell I.D. (in.)
5	100 - 300	100 - 225	7/16
10	100 - 400	100 - 225	7/16
15	100 - 300	100 - 225	7/16
20	100 - 300	100 - 225	7/16
25	100 - 300	100 - 225	7/16
30	100 - 300	100 - 225	7/16
35	100 - 300	100 - 225	7/16
40	100 - 300	100 - 225	7/16
45	100 - 300	100 - 225	7/16
5	100 - 450	100 - 225	7/16
10	100 - 300	100 - 225	7/16
15	100 - 300	100 - 225	7/16

Table 2. Capatively and Inductively-Coupled OES test matrix

Argon Percentage	Pressure [Torr]	Power [Watts]	Discharge Type
5	100	100 - 300	<i>CC</i>
5	100	600 - 800	<i>IC</i>

In order to combine these scans into a single spectra, a wavelength calibration was done. The calibration involved fitting a straight line to the peaks of the Argon, Krypton and Xenon pen lamp spectra to their respective pixel locations as well as using one CC discharge spectrum. Spectral resolutions were simply calculated as the ratio of the wavelength range on the detector and the pixel count of the array. The error in the fits is a measure of the predictive power of the wavelength scale and is dependent on the number of peaks used to fit the axis.

The ICCD detector, connected to the 0.75 m spectrometer, had a spectral resolution of 0.04 nm/pixel. For the ICCD, fit error was less than 0.4 Å except for the last two scans which cover the wavelength range of 880 - 980 nm. The average fit error in these scans is 4.5 Å and 3 Å, respectively. This order of magnitude increase

Table 3. Inductively-Coupled TDLAS test matrix

Argon Percentage	Pressure [Torr]	Power [Watts]
2	10 - 100 at 500 Watts	100 - 600 at 50 Torr
3	10 - 100 at 500 Watts	100 - 600 at 50 Torr
4	10 - 100 at 500 Watts	100 - 600 at 50 Torr
5	10 - 100 at 500 Watts	100 - 600 at 50 Torr
10	10 - 100 at 500 Watts	100 - 600 at 50 Torr
25	10 - 100 at 500 Watts	100 - 600 at 50 Torr

in the error is because of the number of peaks fit, proximity of some spectral lines in the different gases and the change in starting position associated with the mechanical rotation of the grating inside the monochromator.

The InGaAs detector, connected to the 0.3 m spectrometer, had a spectral resolution of 0.25 nm/pixel, about a factor of 6 greater than the ICCD detector. For the InGaAs detector the fit errors have values of 2.3 Å over the range of 700 - 950 nm, 16 Å over the range of 900 - 1150 nm, 9 Å over the range of 1100 nm - 1350 nm and 7 Å over the range of 1300 - 1550 nm. The error in the InGaAs wavelength axis is significantly larger than that of the ICCD detector due to the wide range of the scans compared to a relatively small number of spectral lines as well as the atomic and mechanical problems addressed above.

For the IC OES tests the ICCD spectrometer grating was changed to one with double the groove density and half the blaze and so, as expected, the resolution increased to 0.02 nm/pixel, an improvement by a factor of two.

Microwave spectra was collected at AFIT by Ryan Richards. The spectra were collected using a 0.3 meter monochromator with a 1200 gr/mm and 750 nm blaze. This monochromator has a resolution of 0.03 nm/pixel

The spectra were combined by removing the overlapping data keeping the data associated with the smaller wavelength error. This allows us the individual spectra

to be combined into a single spectrum for each case in the test matrix.

5.3 Blackbody Calibration

In order to calibrate the y-axis a blackbody calibration was performed. The calibration allows us to get a power axis for the spectral lines. Data was collected for a blackbody source at 1000 °C using both detectors. The blackbody spectrum was combined in the same way as the rest of the spectra. Following the combination into a single spectrum, the intensities were adjusted in order to create a single continuous spectrum and the data was smoothed using a 50 point moving average to prevent a large introduction of noise into the data.

The detectivity is then calculated as the ratio of the measured signal, adjusted for integration time, to the Planckian for a blackbody at 1000 °C (1273.15 K). This Planckian is given by (24):

$$L(\lambda) = \frac{2hc^2}{\lambda^5} \frac{1}{e^{\frac{hc}{\lambda k_b T}} - 1} \quad (14)$$

where h is Planck's constant, c is the speed of light, λ is the wavelength, k_b is Boltzmann's constant and T is the blackbody temperature. L is a spectral radiance and so it has units of power per area per unit wavelength per steradian.

The spectral radiance is related to the power per unit wavelength by the equation

$$L(\lambda) = \frac{\partial^2 \phi}{\partial A_{\perp} \partial \Omega} \quad (15)$$

where $\partial A_{\perp} = \partial A_s \cos \Theta_s$ and $\partial \Omega = \frac{\partial A_d \cos \Theta_d}{R^2}$, where A_s is the area of the source and Θ_s is the angle the normal of the source makes with the vector \vec{R} that connects the centers of the two detectors. Similarly, A_d is the detector area and Θ_d is the angle made by the normal of the detector and \vec{R} . A_{\perp} is then the area of the source

seen by the detector and Ω is the solid angle seen by the detector. Using the fact that there is normal incidence, $\Theta_s = \Theta_d$, and using the approximation $R^2 \gg A_s$, the equation can be solved by integrating over the detector and source areas giving the final expression for the power per unit wavelength:

$$\phi(\lambda) = \frac{LA_sA_d}{R^2} \quad (16)$$

If this radiometrically adjusted radiance is divided by the blackbody signal, S_d , which has units of counts/pixel, by its integration time and the power above, we get the detectivity:

$$D = \frac{S_d}{\tau_d \Phi(\lambda)} \quad (17)$$

which has units of counts-unit wavelength per joule per pixel. In order to get this into the right units it must finally be multiplied by the reciprocal of the spectral resolution which has units of wavelength per pixel. Furthermore, if the spectrum, which has units of counts, is divided by its integration time and the detectivity, the result is a calibrated y-axis with units of watts. The blackbody curve and detectivity for the InGaAs is shown in Figure 10 and for the ICCD in Figure 11.

5.4 Fluorescence Spectra

Spectra were collected using both the ICCD and InGaAs detectors. All expected dipole allowed transitions were observed. The full assignment, including the upper and lower levels using Paschen notation, is provided in Figure 12.

These spectra are a result of the kinetics of the discharges. Different intensity distributions for the spectral lines relate to different populations in the excited state. These spectra can be used to inform the kinetic changes that occur for a large number

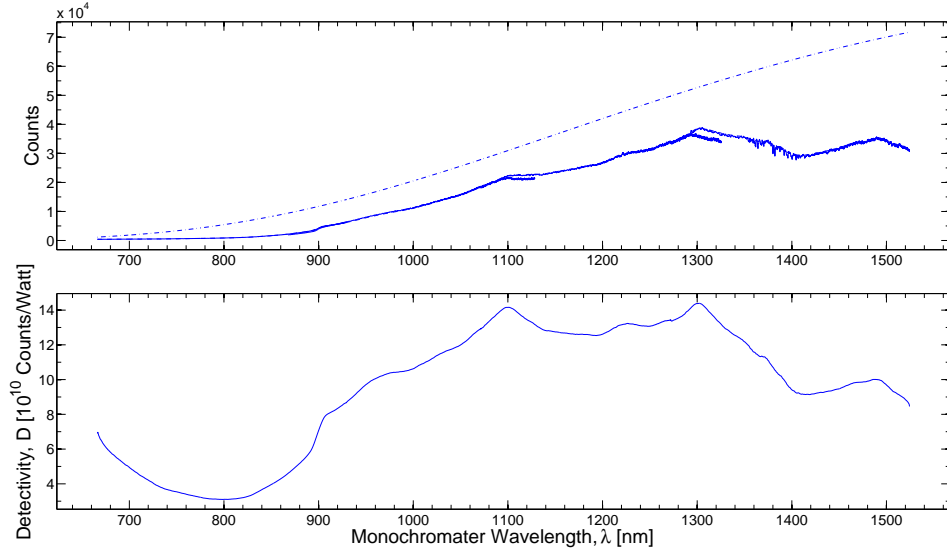


Figure 10. The 1000°C blackbody spectrum for the InGaAs detector is shown as the original separated data, the solid line, the combined, smoothed blackbody data, the dotted line, and the radiometrically adjusted Planckian in units of Watts, the dash-dot line. The Planckian has been multiplied by 10 to be visible on the scale of the blackbody curve. Below it is the detectivity, in 10^{10} counts/Watt.

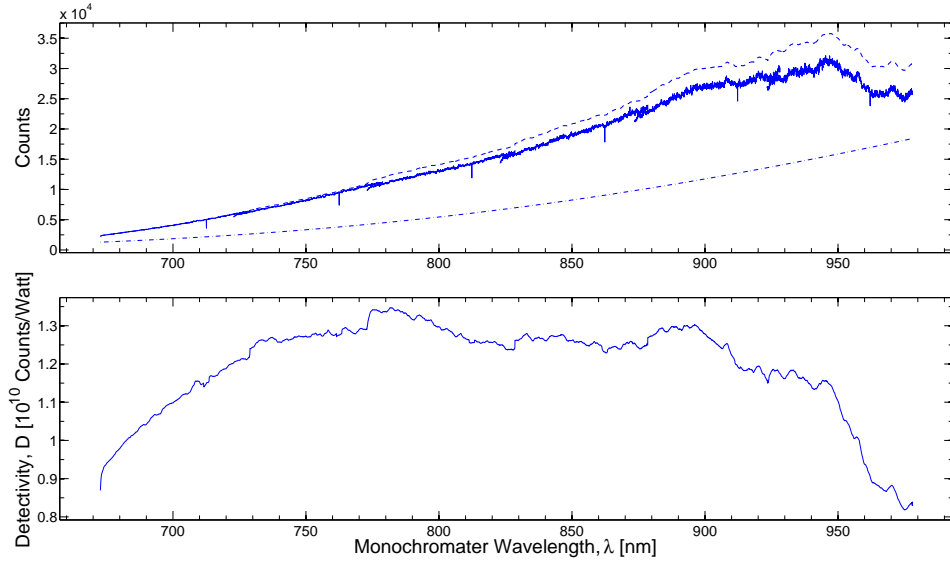


Figure 11. The 1000°C blackbody spectrum for the ICCD detector is shown as the original separated data, the solid line, the combined, smoothed blackbody data, the dotted line, and the radiometrically adjusted Planckian in units of Watts, the dash-dot line. The Planckian has been multiplied by 10 to be visible on the scale of the blackbody curve. Below it is the detectivity, in 10^{10} counts/Watt.

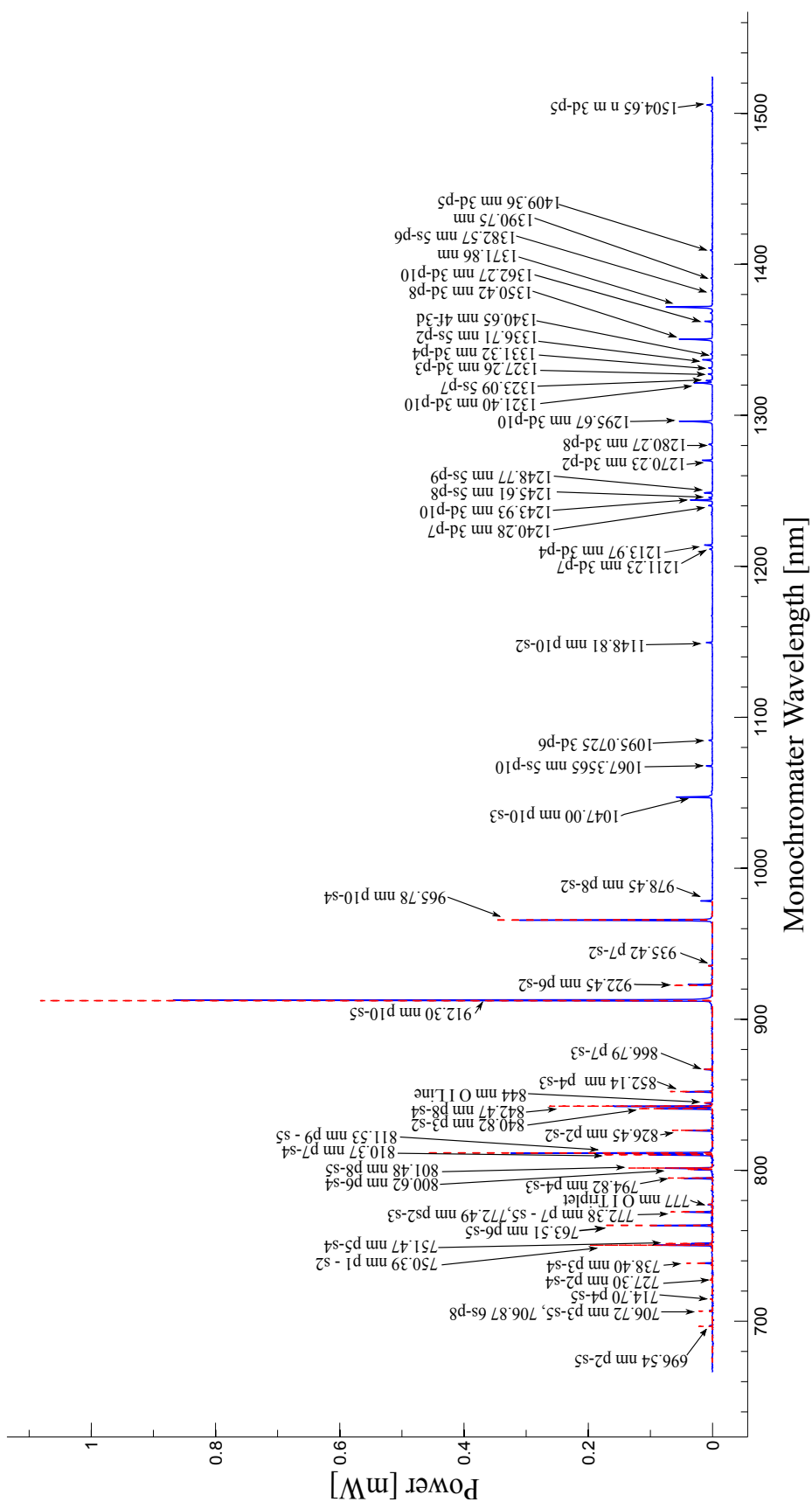


Figure 12. The argon discharge spectrum is shown, fully assigned, including a few atomic oxygen lines. All dipole and spin allowed transitions are accounted for. The ICCD signal was multiplied by 2 in order for the weak lines to be visible for assignment. These spectra were collected from the Ar/He discharge with a 5% argon mixture at 100 Torr and 100 Watts.

of discharge types and conditions. First, in Figure 13 the variations in the spectra for a CC discharge at 5% argon for three different pressure and power levels is compared.

The spectra shows some interesting behavior as both the pressure and power are increased. Some of the spectra lines decrease in intensity while others increase informing the complex relationship between the production and destruction rates of the excited states and how they depend on the gas pressure, electron density and electron temperature. The increases in pressure can both reduce the excitation rate, by decreasing the electron temperature in the discharge, or the destruction rate, by increasing the quenching rate. The increase in RF power, however, only really increases production by increasing the electron temperature. There is little quenching associated with it as the superellastic collisions required to quench the excited states with electrons have small cross-sections. A look at these spectra show that as the pressure and power change the 826.45 nm p2 line as well as the 750.39 nm p1 and 751.47 nm p5 pair and the 800.62 p6 and 801.48 nm p8 pair all decrease in intensity. The 840.82 p3 and 842.47 nm p8 pair increase in intensity, as do the 810.37 nm p7 and 811.53 nm p9 pair. The excitation and destruction kinetics are what impact these spectral line intensities for which there is no clear trend. Quenching rates are expected to increase linearly with increasing pressure which should be even across all states. That fact reveals that the lower states are more sensitive to increases in RF power, increasing in population despite the increase in pressure compared to the higher states which only show a reduction in population. It is also worth noting that both the 844 nm and 777 atomic oxygen triplets decrease in intensity.

Next four different discharge configurations are compared: a capacitively-coupled discharge with 5% argon at 100 Torr and 100 Watts, an inductively-coupled discharge with 5% argon at 100 Torr and 600 Watts, a microwave discharge with 5% argon at 100 Torr, and an argon pen lamp in Figure 14.

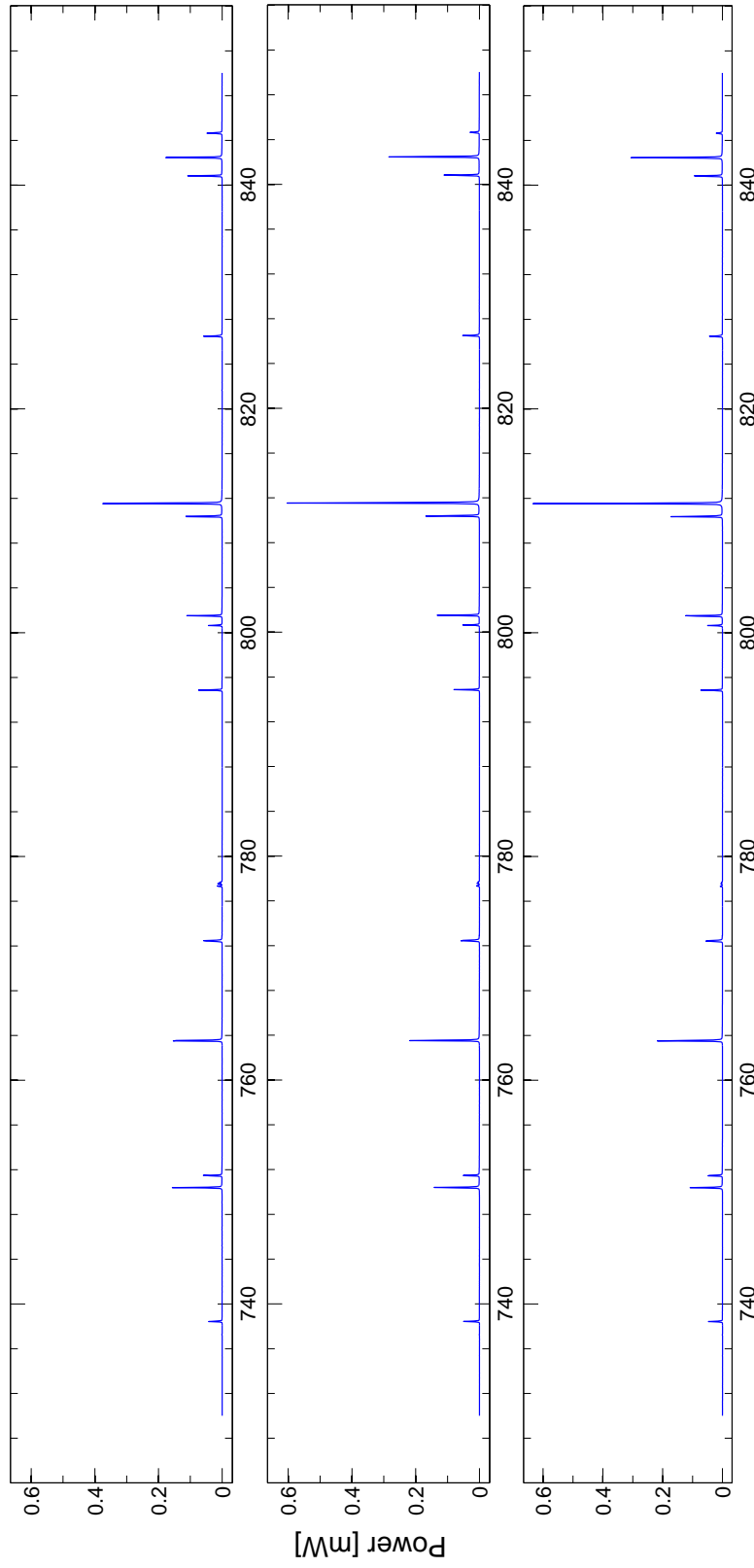


Figure 13. The CC discharge shown are for a CC discharge with 5% argon at 100 Torr and 100 Watts, top, 200 Torr and 150 Watts, middle, and 300 Torr and 200 Watts, bottom. Some spectral lines increase in intensity, specifically 763.51 nm, 810.37 nm, 811.53 nm, 840.82 nm, and 842.47 nm. The other spectral lines have decreasing intensities, 750.39 nm and 751.47 nm, or remain essentially the same, 826.45 nm and the 844 nm atomic oxygen triplet

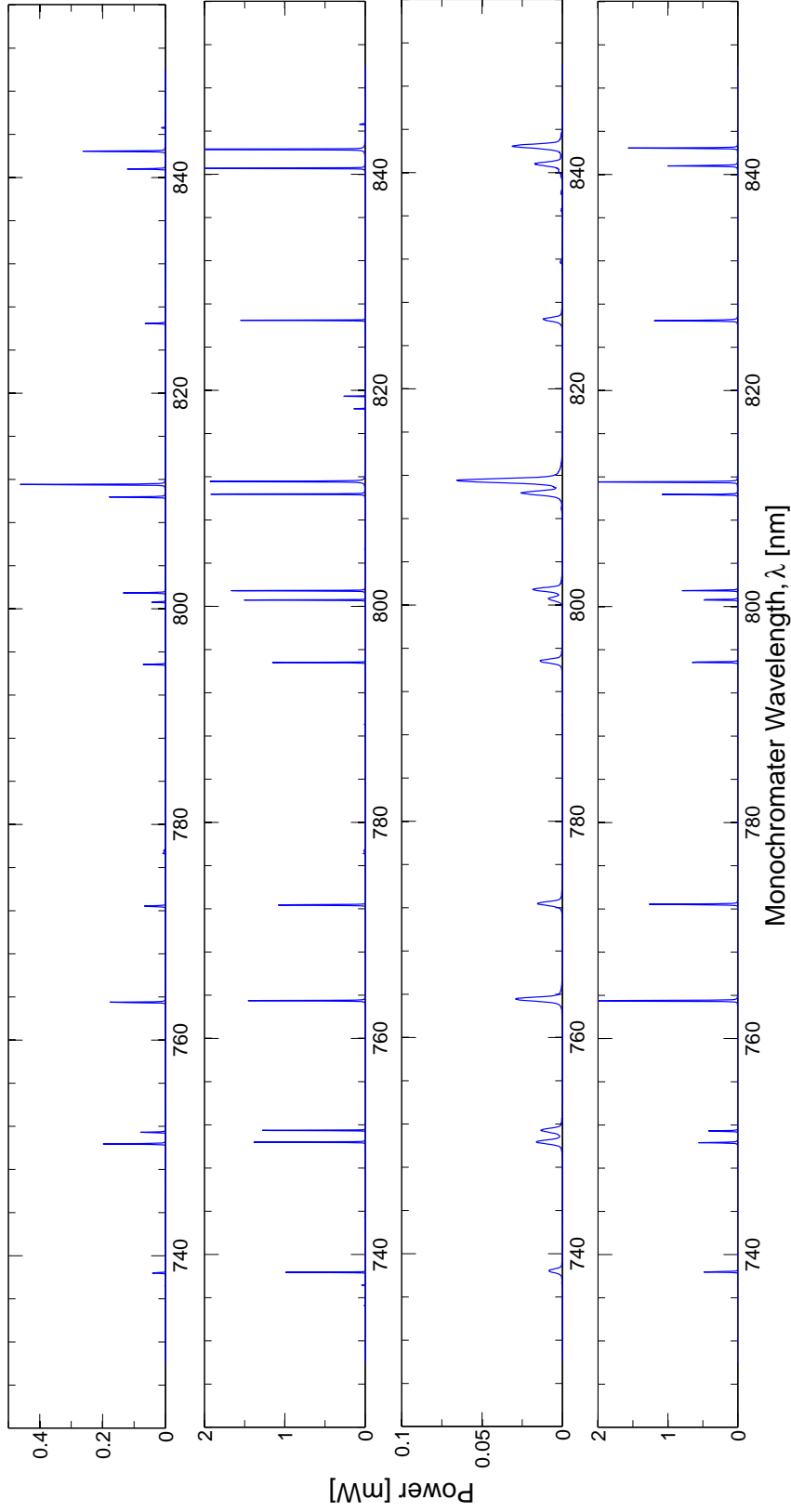


Figure 14. The above four spectra show a wide variety in the intensity distribution of the spectral lines in the 750 - 850 nm range. The discharges, in order from top to bottom, are a capacitively coupled radio-frequency discharge with 5% argon at 100 Torr and 100 Watts, and inductively coupled radio-frequency discharge with 5% argon at 100 Torr and 600 Watts, a microwave discharge with 5% argon at 100 Torr and an argon pen lamp. These different intensity distribution point to different dominant mechanisms in the discharge kinetics.

The intensity distribution of the lines varies fairly significantly between the four spectra. The microwave spectrum had wider spectral lines due to the instrument resolution and lineshape. A comparison of the pairs of lines about 750 nm, 800 nm, 810 nm and 840 nm provides some field for comparison of the spectra. Those lines and the transitions they are emitted from are given in Table 4.

Table 4. A comparison of some closely spaced spectral lines and the transitions from which they are emitted

Wavelength [nm]	Transition in Paschen notation
750.39	p1 \rightarrow s2
751.47	p5 \rightarrow s4
800.62	p6 \rightarrow s4
801.48	p8 \rightarrow s5
810.37	p7 \rightarrow s4
811.53	p9 \rightarrow s5
840.82	p3 \rightarrow s2
842.47	p8 \rightarrow s4

We see that the line ratios are consistent between the microwave and argon pen lamp spectra. This tells us that the kinetics of the two discharges are similar and will have similar excited state population distributions. The CC discharge is the next closest with the 800 nm, 810 nm and 840 nm line ratios the same as the bottom two spectra. The 750 nm line ratio, however, is significantly different with the 750.39 nm line being much more intense than the 751.47 nm one. This tell us that the CC discharge produces more of the p1 state. This increased production is reasonable to expect as the CC discharge runs at higher powers than either the microwave discharge or the argon pen lamp. The p1 state is the highest lying p-state and so it would require a higher electron temperature in the discharge in order to be excited. Finally, the IC spectrum is the most different with all the line ratios close to 1. This is not a result of a line saturating the detector as being below saturation was insured. The

IC discharge appears to be producing significantly more population in all the levels when compared to the other three discharges.

5.5 Population Distribution

From the collected spectra effective population distributions were derived as well as electronic temperatures, by the method described in Chapter 2. In this case the temperature parameter in the Boltzmann term is the electronic temperature. The populations vary for different discharge configurations, gas mixtures, and pressures which implies that different mechanisms dominate the production and the destruction of the excited states. The effective populations are plotted as a function of the upper state energy in Figure 15 with the intention of fitting a line to extract that temperature.

The InGaAs spectral lines provide more information about the d-state population distribution whereas the ICCD spectral lines provide information about the p-state population distribution. This is because most of the 3d to 4p transitions fall in the NIR and the 4p to 4s transitions are between the visible and NIR. The population distributions are clearly non-statistical with the 3d state appearing more widely distributed than the 4p states. The non-statistical nature implies either the equilibrium kinetics of the argon and electrons in the discharge are non-Maxwellian, the populations even at equilibrium would not be representative of a Maxwell-Boltzmann distribution, or that the system is in a non-equilibrium state. The error in these points arises not from the noise or any systematic error but from the error involved in the Einstein A coefficients which are 25% for the lines that originate on the 4p states and range from 25% to 50% for the spectral lines that originate on the 3d states(25). Upon further examination of the p-state distribution it becomes apparent that the spectral lines that terminate on metastable states underestimate the population of the

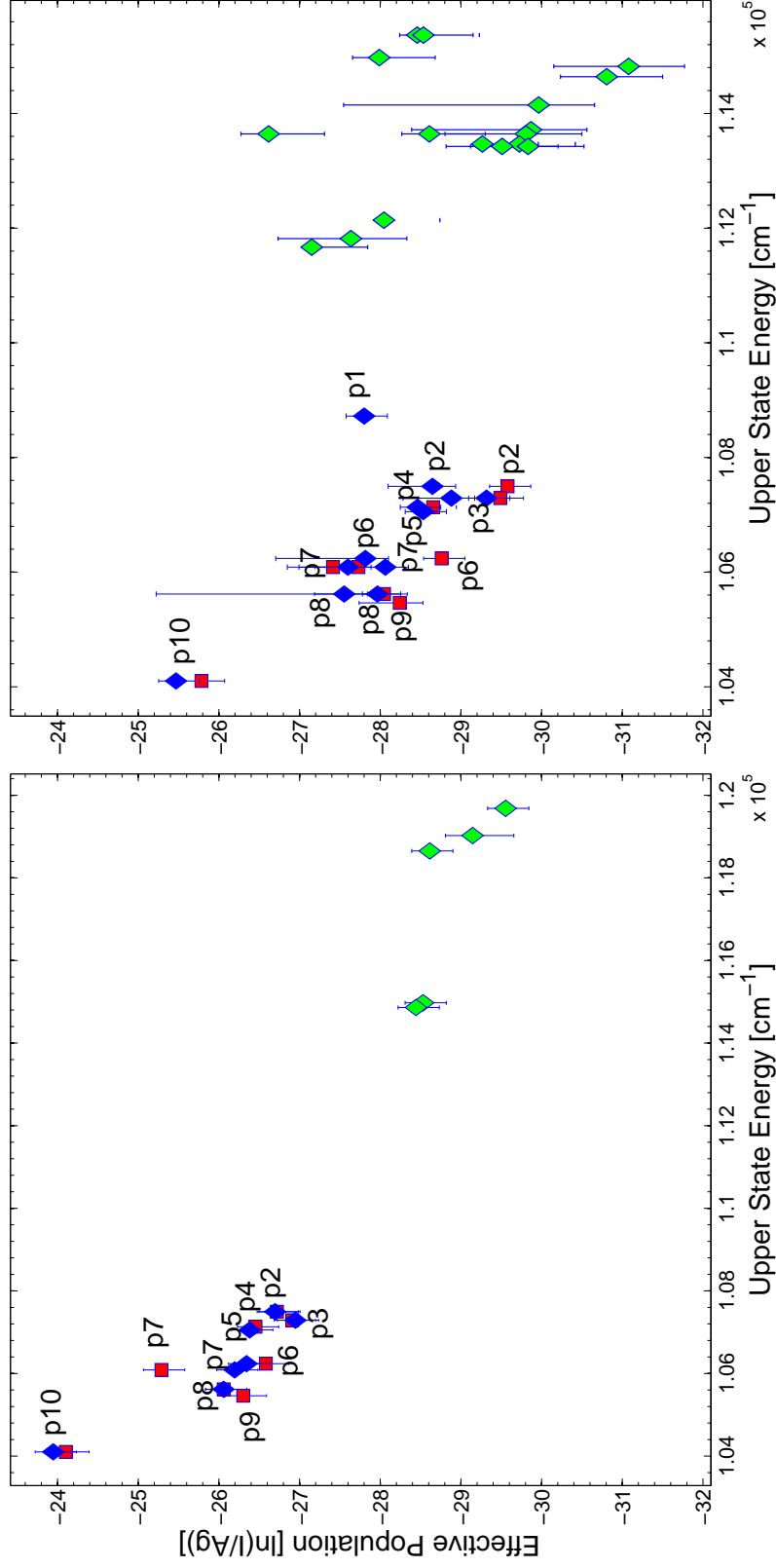


Figure 15. The squares, \square , are calculated populations for lines that terminate on metastable states, the diamonds, \diamond , are for lines that terminate on resonance states, and the green are for higher lying states. The left figure shows the population distribution of the InGaAs spectrum. The right figure shows that of the ICCD spectrum. Clearly, the InGaAs spectrum contains a significant number of higher state populations which appear to be non-statistical, whereas the ICCD spectrum contains more p-state populations which appear to be nearly statistical.

upper state. This is true for all but the p7 state for which the opposite is true. This trend is consistent across all the data and likely occurs because of radiation trapping in the cell. The reason that the p7 state is reversed may be due to the kinetics of the p7 state but is more likely due to the incorrect A coefficient. The Einstein A Coefficients are not known to good statistical accuracy and may potentially be entirely incorrect. The difference in the populations does not arise from the spectral line being in a low detectivity region as all the p7 - s transitions fall in within the spectral response of the ICCD. In order for there to be radiation trapping in the cells there must be a large concentration of metastables which would be ideal for the design of the laser system.

The question of radiation trapping is worth further investigation. An examination of these population distributions for different discharge conditions can reveal the existence of this phenomena. Figure 16 shows the population distributions of the CC discharge at 100 Torr and 100 Watts on the left and 300 Torr and 200 Watts on the right.

The p6 state gives the best evidence for radiation trapping as both the metastable and resonance transitions are present. The population of the metastable transition drops significantly as the pressure rises to 300 Torr and the power to 200 Watts. This is most likely due to absorption of the emitted light by the metastables. A comparison of the CC and IC population distributions can be found in Appendix D.

In order to extract an approximate electronic temperature, a linear fit to the p-state distribution was done and is shown in Figure 16. The clearly non-Maxwellian nature of the population distribution and the exclusion of the higher lying states are the reasons, among others, for why the temperature is only an estimate. The p10 state has a much larger population than a Boltzmann distribution would imply and so a single temperature fit is insufficient. Instead, a two-temperature fit, the p10 -

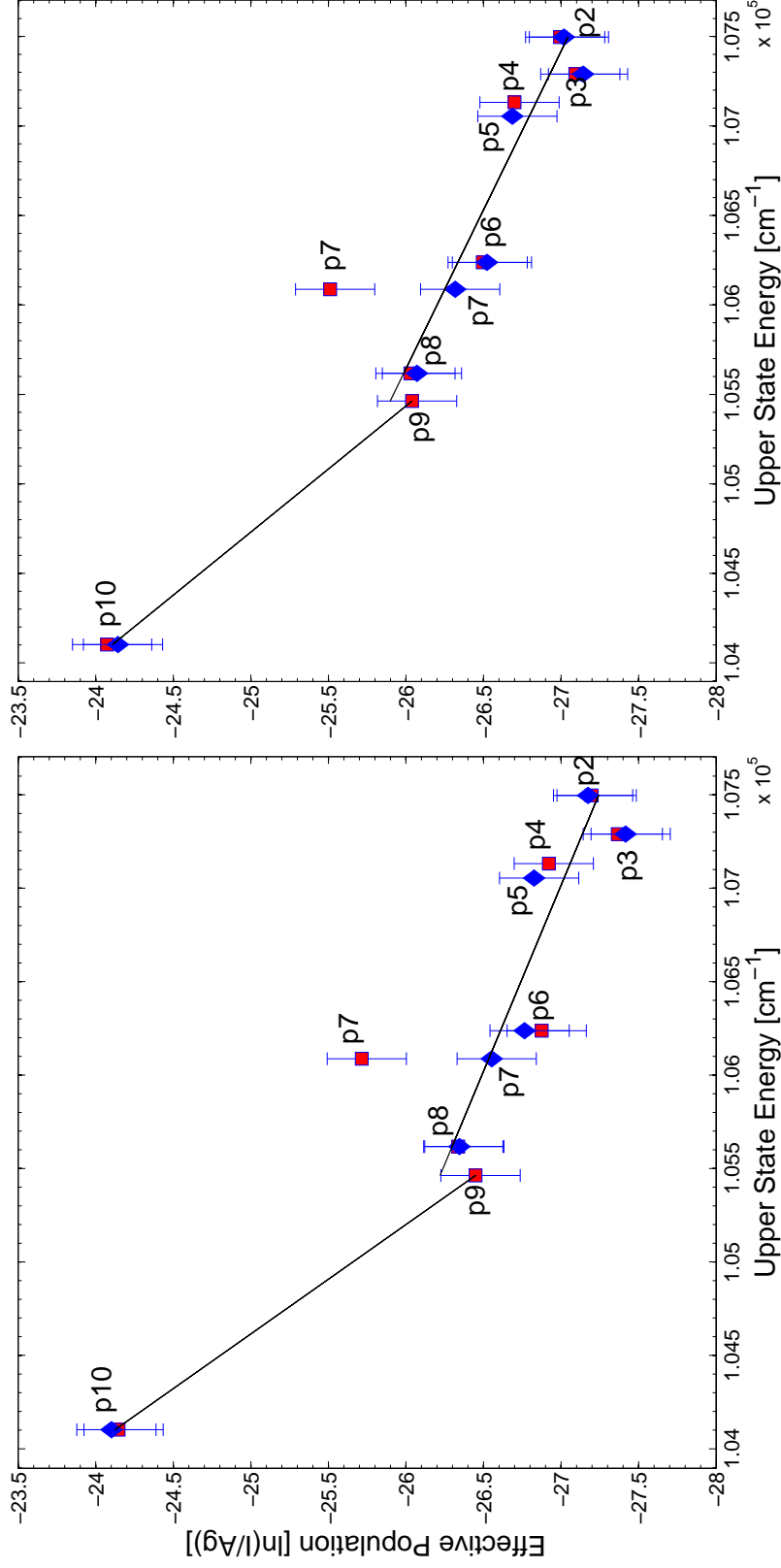


Figure 16. The squares, \square , are calculated populations for lines that terminate on metastable states, the diamonds, \diamond , are for lines that terminate on resonance states. The left plot shows the temperature fit to the p-state population for the CC discharge at 100 Torr and 100 Watts and the right plot is for the CC discharge at 300 Torr and 200 Watts. Both plots show a common trend, the p10-p9 state electronic temperature is lower than the p9-p1 state electronic temperature.

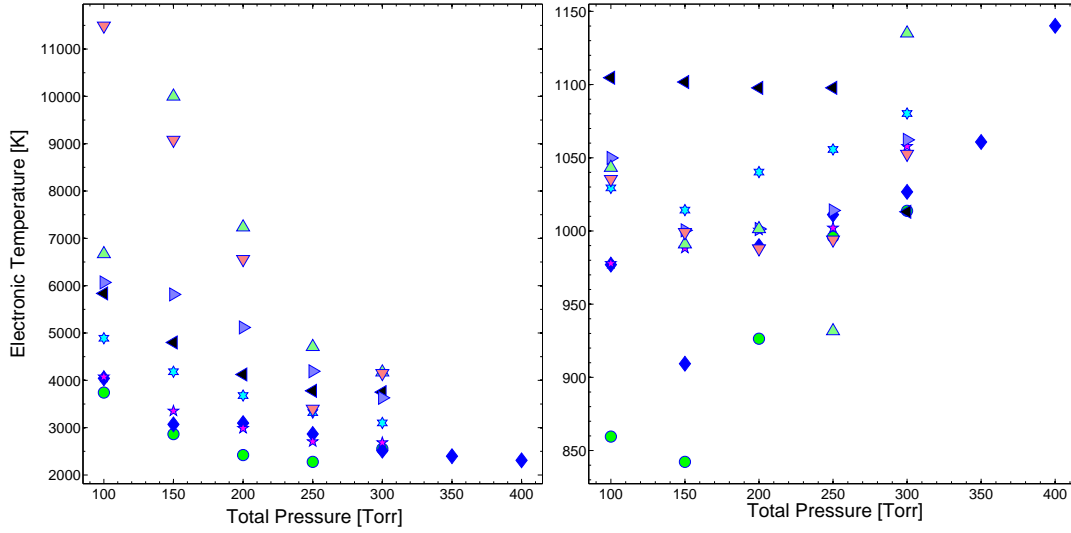


Figure 17. The electronic temperatures are shown for the p9-p1 state, left, and the p10-p9 state, right, for multiple argon mixtures. The p9-p1 state temperatures trend downwards from approximately 11,000 K to 3,500 K. The p10-p9 state temperatures are significantly lower, around 1100 K, and do not show any significant trends. Some of the populations trend upwards but this is not a consistent trend in the data. The argon mixtures are represented by the different markers as follows: 5% argon - \square , 10% argon - \diamond , 15% argon - \diamond , 20% argon - \star , 25% argon - \star , 30% argon - \triangleleft , 35% argon - \triangleright , 40% argon - \triangle .

p9 states and the p9 - p1 states, was used to examine the two separate trends. The temperature trends shown in Figure 17 are derived only from the ICCD data as it contains the largest number of p-state population points.

Interestingly, the electronic temperature of the p9 - p1 state temperature decreases with increasing pressure but increases with increasing argon percentage. This may be due to the lower ionization energy of argon relative to helium. The ionizing electrons do not need to have as much kinetic energy and will, therefore, lose less kinetic energy in those collisions. The overall effect would be to increase the mean energy of the electrons which is what we are estimating with these electronic temperatures. The p1-p9 temperature also appears to move towards a constant value, different for each mixture. This may mean that the gas in the discharge is approaching an equilibrium as the pressure is increased. This equilibration points to the role that helium plays

in the argon-helium discharge. As the total gas pressure, which is predominantly helium, is increased the population distributions of the p states approach a Boltzmann distribution. The trend implies that the helium is mixing the population of the states at a rate which approaches the non-Maxwellian production and destruction rates of the argon states in the discharge and is forcing them into a Boltzmann distribution. Unfortunately, there is no definitive trend in the p10-p9 electronic temperature. It appears to be increasing with increasing temperature but is too scattered to allow any definite statements.

Another important consideration is on the impact of Helium on the excited state distribution. Comparing the CC and IC p-state distributions to Optical Emission Spectroscopy measurements made by Zhu, et. al. (26) reveals the large impact that helium has in Figure 18.

The populations of the high pressure, high power IC and CC discharges are in great contrast to the population distribution in lower pressure, low power, pure argon IC and CC discharges as measured by Zhu, et. al. The different population distributions are explained by the fact that the kinetics of the argon helium discharge are quite different from that of the pure argon discharges of the same configuration. The mechanisms by which helium moves population around in the excited argon states is unknown, a problem that is yet to be addressed.

5.6 Absorption Spectra

Absorption data was collected for a wide range of test conditions in the IC discharge. This data can be categorized into two separate sets, one that keeps the pressure fixed and varies the RF power allowing for an analysis of the Doppler width and estimations of the plasma temperature, and the second which keeps the RF power fixed and changes the pressure allowing for a study of the Lorentzian width and an

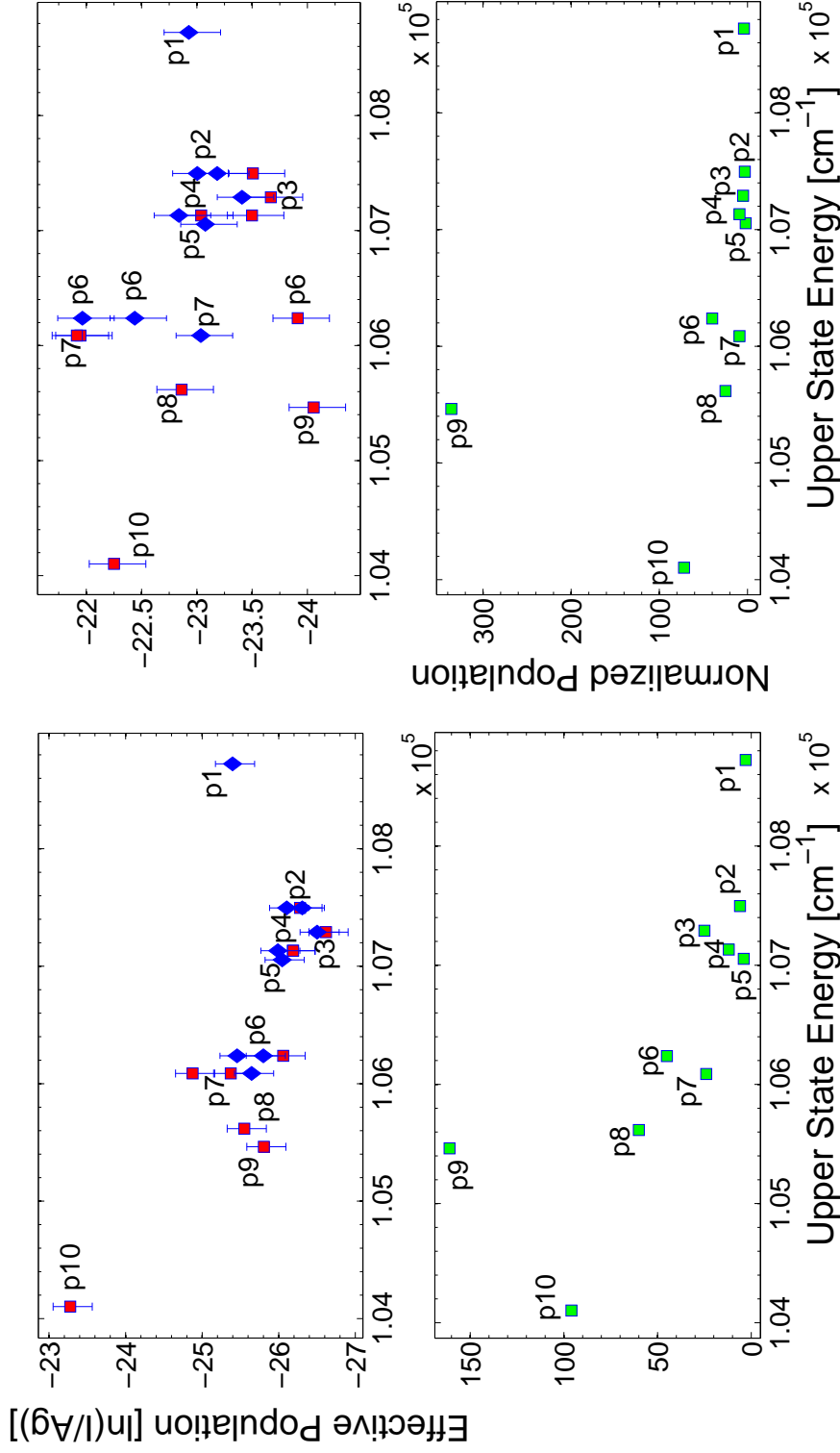


Figure 18. The impact of helium on the argon discharge is apparent. The left plot compares a capacitively coupled argon-helium discharge at 100 Torr and 300 Watts to a pure argon discharge of the same type at 120 Pascal (900 mTorr) and 50 Watts. The right plot compare an inductively coupled argon-helium discharge at 100 Torr and 600 Watts to a pure argon discharge of the same type at 1 Pascal (7.5 mTorr) and 75 Watts. The population distributions are significantly different representing the large impact that helium has on the population distribution.

extraction of pressure broadening rates. This data was fit using the approximation to the Voigt line-shape defined in Chapter 2. The approximation is given by

$$g(\nu) = 2\sqrt{\frac{\ln(2)}{\pi}} \frac{1}{\Delta\nu_D} \text{Re}[w(iz)] \quad (18)$$

where $w(z)$ is the Faddeeva function defined as $w(z) = e^{-z^2} \text{Erfc}(-iz)$ (21) and the parameter z is defined as $z = a + iu$ where

$$a = \sqrt{\ln(2)} \frac{\Delta\nu_L}{\Delta\nu_D} \quad (19)$$

$$u = 2\sqrt{\ln(2)} \frac{\nu}{\Delta\nu_D} \quad (20)$$

The approximate Voigt profile was fit to the data recursively. For low pressures the absorbance was significantly higher than the system can detect. The data was excluded in order to fit the maximum amount without allowing the low-detectivity, central region to interfere with the fit. The reason for the large exclusion region is in the unknown behavior of the photo-diode at low signal strength. The detector is known to have a linear response in normal signal ranges but behavior at extremely low signal was unexplored. A higher detectivity would have been accessible if the detector was connected to a voltage amplifier. Since most of the information of the Voigt profile is contained in the wings, the exclusion of data in the center of the scan is not expected to greatly impact the fidelity of the fit. In addition to the exclusion of the data, a fit where both the Lorentzian and Doppler widths were allowed to float was conducted. This fit allowed for an examination of the variation in the two parameters across the data. The wide variation in the two parameters required fixing of one parameter while allowing the second to float. For the data in which the pressure was varied the Doppler width was fixed and the Lorentzian width is floating and vice versa for the power varying data. Since the power broadening data is all

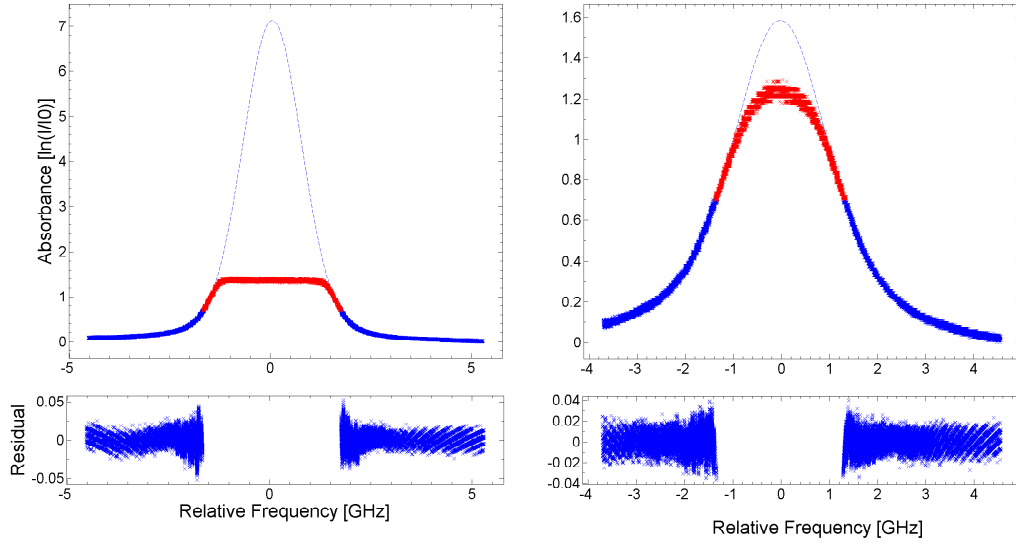


Figure 19. The fits are for an IC discharge with 5% argon at 500 Watts and 10 Torr, left, or 100 Torr, right. Apparent structure in the fit residuals arises from striation in the data.

conducted at 50 Torr an estimate of the Lorentzian width at 50 Torr of 0.95 GHz was used. For the pressure broadening data a Doppler width of 1.6 GHz was fixed, which corresponds to an approximate plasma temperature of 1350 K. Both of these estimates for the widths were derived from the recursive analysis for obtaining the fits. A more appropriate method for the Doppler and Lorentzian widths would take into account the variation of the widths with temperature. The Lorentzian width varies as $\frac{1}{\sqrt{T}}$ and the Doppler width varies as \sqrt{T} , so fixing these parameters is, strictly speaking, a rough approximation. The plasma temperature is expected to depend on both the gas flow rate, which is increased for the pressure to increase, and the RF power. In Figure 19 the quality of the Voigt fit for a low pressure and high pressure case are shown for the 801.48 nm transition that terminates on the metastable s5 state. The 794.82 nm transition that terminates on the metastable s3 state was fit similarly and can be seen in Figure 20.

The fits show larger residuals towards the edge of excluded data. These residuals

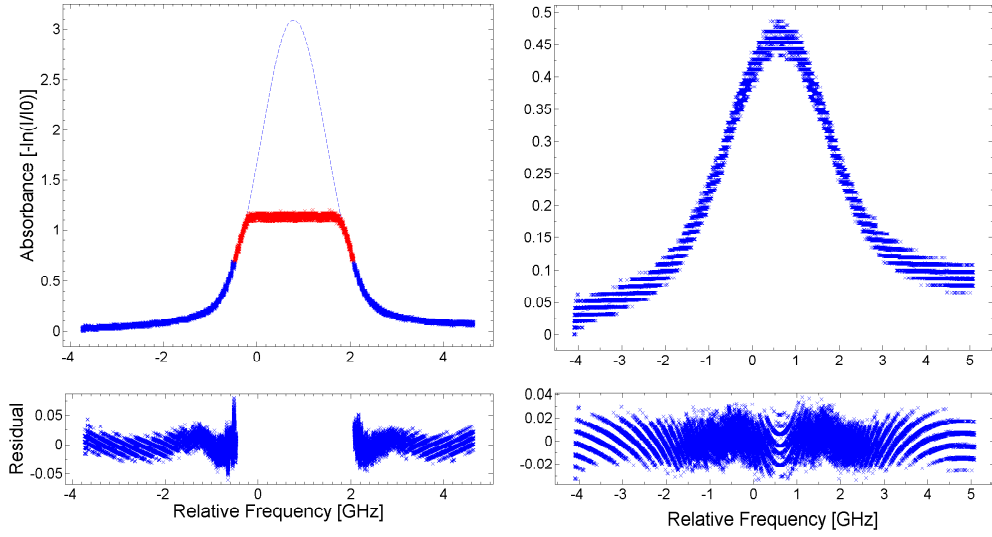


Figure 20. The fits are for an IC discharge with 5% argon at 500 Watts and 10 Torr, left, or 100 Torr, right. Apparent structure in the fit residuals arises from striation in the data.

and the apparent structure arise from the striation in the data and the magnitude of the residuals come from the striation width of about 0.04 in absorbance. Better data, for which I , the measured signal after transmission through the cell, and I_0 , the measured signal before entering the cell, were properly matched, the RF noise was removed, and a more robust exclusion method that accounts for the baseline was included, would lead to a better fit.

From the Doppler and Lorentzian line-widths an approximate temperature trend and the pressure broadening rate can be derived. First, the trend in the Lorentzian width is examined. In Figure 21 the Lorentzian FWHM appears to increase linearly for both the s5, right, and s3, left, transitions.

The pressure broadening rate is the slope of these linear increases and so a single line is fit to the pressures in order to calculate an approximate pressure broadening rate. The broadening rate is different for the different argon percentages and is likely due to the combination of the low fidelity of the data and other broadening

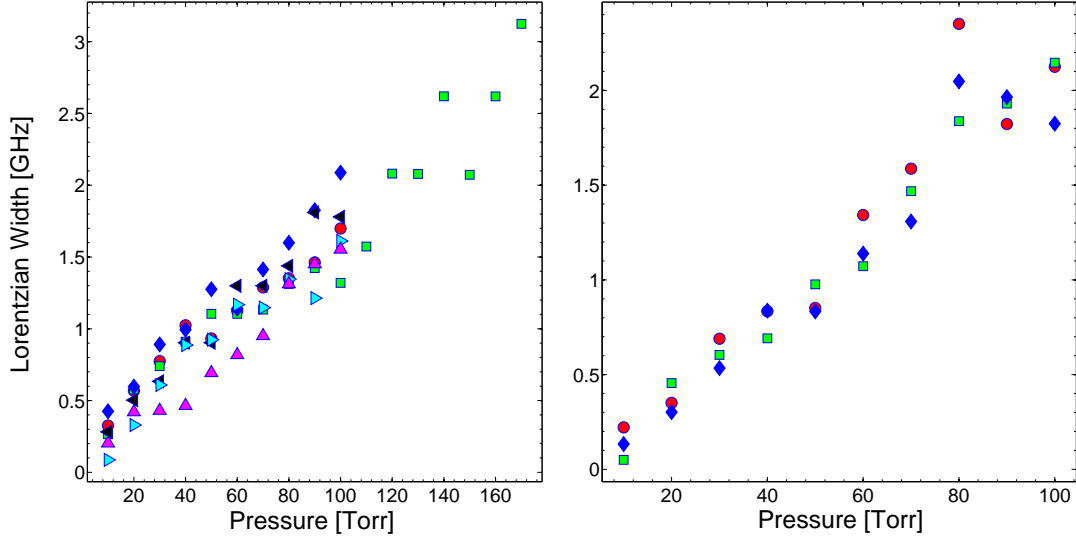


Figure 21. The line-width, as measured by the Voigt fit, increases as the total gas pressure rises. The line-width for the s5 transition ranges from 1.5 GHz to 3.2 GHz, and from 0.25 to 2 GHz for the s3 transition, as the pressure rises from 10 to 100 Torr. The symbols correspond to argon mixtures as follows: 2% argon - \circ , 3% argon - \square , 4% argon - \diamond , 5% argon - \triangleright , 10% argon - \triangleleft , 25% argon - \triangleright .

mechanisms associated with the plasma such as electron broadening and resonance broadening. The pressure broadening rates are given in Table 5 and Table 6. The average broadening rates are 18 ± 5.8 MHz/Torr and 22 ± 1.2 MHz/Torr for the s5 and s3 transitions, respectively.

Table 5. Pressure broadening rates for the s5 metastable state

Argon Percentage	Broadening Rate [MHz/Torr]
2	17 ± 2.4
3	19.0 ± 0.9
4	15.7 ± 0.9
5	20 ± 2.9
10	19 ± 3.8
25	15 ± 1.9

Any trends in the Doppler widths can also be examined. These widths are plotted as a function of RF power in Figure 22.

Table 6. Pressure broadening rates for the s3 metastable state

Argon Percentage	Broadening Rate [MHz/Torr]
2	23.1 ± 0.9
3	22.3 ± 0.4
4	22.1 ± 0.8

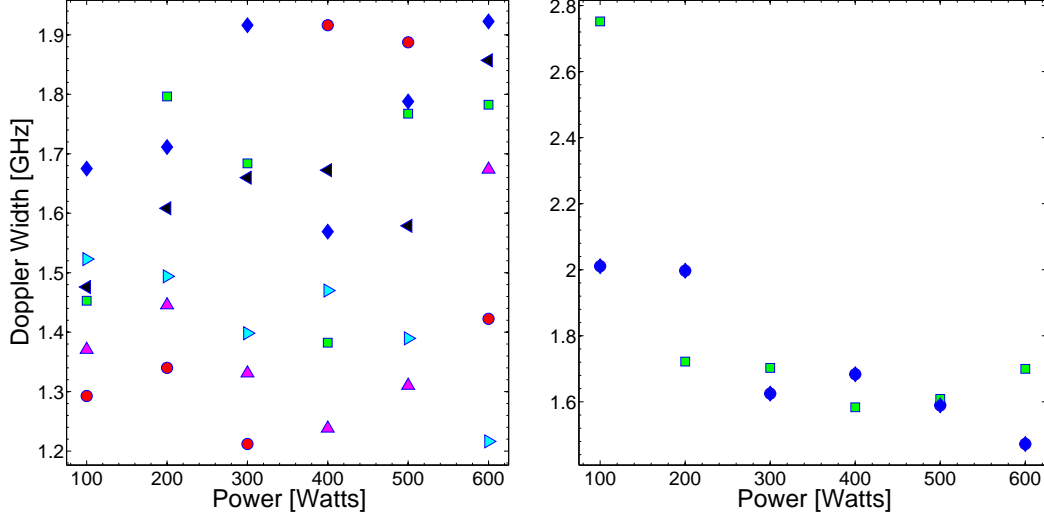


Figure 22. The line-width, as measured by the Voigt fit, is scattered as a function of RF power. The line-width ranges from 1.2 to 1.9 GHz for the s5 metastable transition, and 1.5 to 2 for the s3 metastable transition, as the power rises from 100 to 600 Watts. The symbols correspond to argon mixtures as follows: 2% argon - \circ , 3% argon - \square , 4% argon - \diamond , 5% argon - \triangleright , 10% argon - \triangleleft , 25% argon - ∇ .

Unfortunately, there is no clear trend in the Doppler width. Solving the equation of the Doppler width for the temperature using the above widths provides a temperature range for the plasma. The temperature is given by

$$T = \frac{mc^2}{2k_b} \left(\frac{\Delta\nu_D}{2\nu_0} \right)^2 \quad (21)$$

The temperature range for the plasma given by the large scatter in the plasma widths as 1000 K to 2300 K corresponding to Doppler widths between 1.4 GHz and 2.1 GHz. The s3 range is slightly narrower, between 1.6 and 2.1 GHz, giving a temperature

range of 1300 K to 2300 K and providing evidence for real plasma temperatures in the higher part of the estimated range.

In addition to the study of the Doppler and Lorentzian widths, the Voigt fits give an estimate for the peak absorbance as a function of both pressure and power. This provides allows for an examination of the metastable column densities as they trend with pressure and power for the different percentages of argon in the Ar/He plasma. A column density, not a number density, is the only quantity that can be calculated. Despite the fact the total fluorescing length of the discharge was tracked approximately, there were sections of the discharge blocked from view and so the full discharge length trend is unknown. Using Beer's Law for the transmission, the column density is given by:

$$Nl = -\frac{1}{\sigma(\nu_0)} \log\left(\frac{I}{I_0}\right) \quad (22)$$

The above cross-sections come from evaluation of the approximation of the Voigt profile at line-center. In the above derivation of the Voigt approximation the term ν is a relative frequency and can be written $\nu - \nu_0$. At line-center the Voigt line-shape evaluates to

$$g(\nu_0) = 2\sqrt{\frac{\ln(2)}{\pi}} \frac{1}{\Delta\nu_D} \text{Re}[w(ia)] \quad (23)$$

We note that $u = 0$ when $\nu = \nu_0$ and so $z = a$. The absorbance and column density as they trend with pressure for the s5 metastable state is shown in Figure 23 and for the s3 metastable state in Figure 24.

The absorbance and column density both decrease as the pressure increases. This is an unexpected conclusion as the discharge continues to fluoresce brightly. The number density in the discharge should stay relatively constant. It was previously

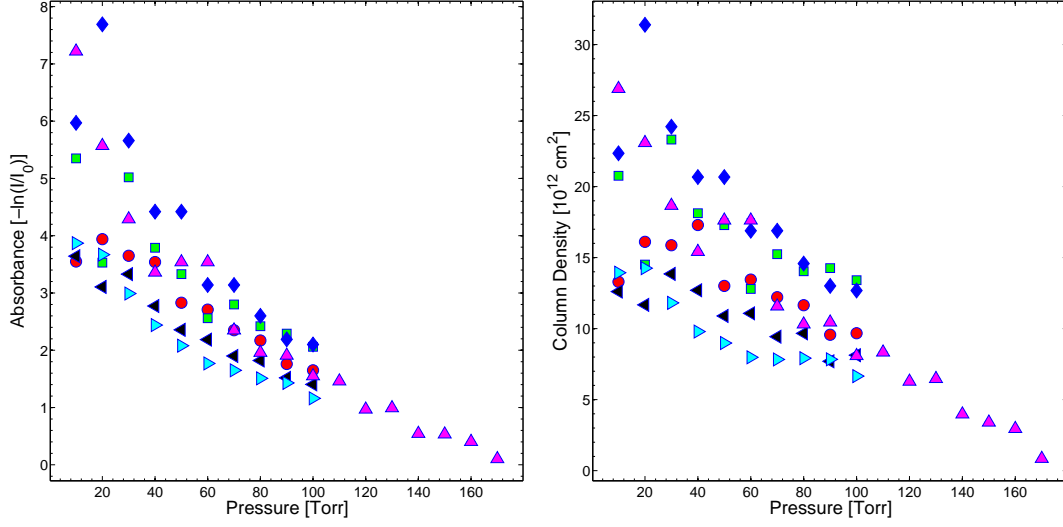


Figure 23. The absorbance of the s5 metastable state, left, shows a distinct trend, as pressure increases the absorbance decreases. When a line-width adjusted cross-section is used to calculate the column density, right, the trend becomes less distinct but is still apparent. The argon mixtures are represented by the different markers as follows: 2% argon - \circ , 3% argon - \square , 4% argon - \diamond , 5% argon - ∇ , 10% argon - \star , 25% argon - \ast

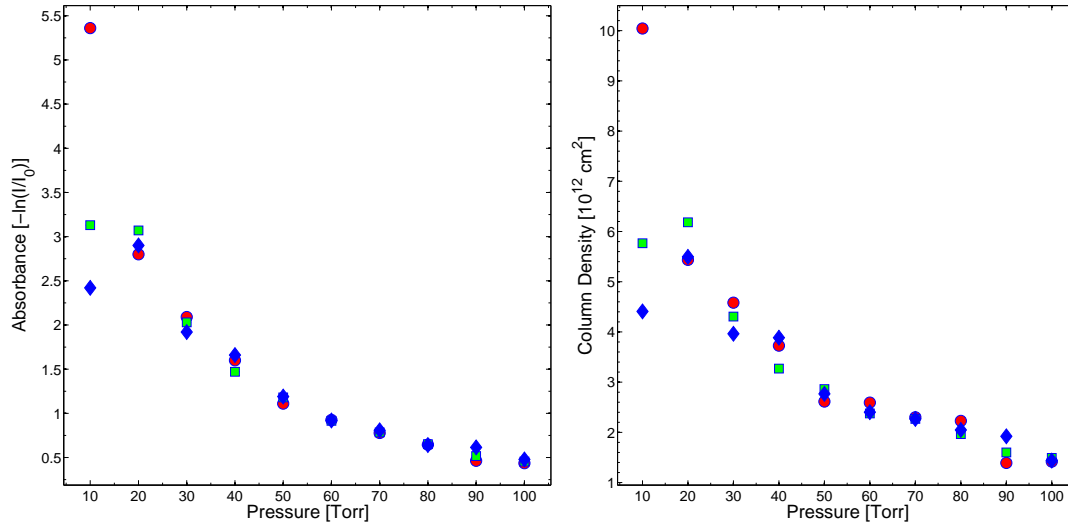


Figure 24. The absorbance of the s3 metastable state, left, shows a distinct trend, as pressure increases the absorbance decreases. When a line-width adjusted cross-section is used to calculate the column density, right, the trend becomes less distinct but is still apparent. The argon mixtures are represented by the different markers as follows: 2% argon - \circ , 3% argon - \square , 4% argon - \diamond

noted, however, that the discharge length decreases as the pressure increases. These decreases in the column density are likely due to the decrease in this discharge length. The discharge length decreases from the full cell (≈ 60 cm) to (≈ 20 cm). This factor of three decrease in the discharge length alleviates the factor of three decrease in column density seen in the 794.42 nm, s3 transition and the factors of two to three decrease in the column density of the 801.48 nm, s5 transition. An inclusion of the discharge length will give a number density that, as expected, will remain constant.

In contrast to the expected stability of the metastable number density with changes in pressure, the density is expected to increase with RF power. As the RF power is increased the electric field in the discharge should increase, increasing the electronic temperature and density of electrons. There should be a corresponding change in the number density as the production rates are functions of the electron density and temperature. The absorbance and column density of the s5 and s3 metastable states are shown in Figure 25 and Figure 26.

The column densities of the s5 and s3 states increase by factors of 2 and 7, respectively. This shows the difference in sensitivity of the s5 and s3 metastable concentrations as the power increases, that is, the production rate of the s3 state is a much stronger function of the RF power. For a full understanding of the metastable concentration the discharge length must again be considered. As the RF power changes from 200 W to 600 W the discharge length would be expected to increase, which it does. This increase, however, is relatively small. As the power increases from 200 - 600 Watts the discharge length increases by 25%. The behavior of the discharge length in response to RF power is not smooth at low RF powers where the discharge is not strongly lit. In this regime the discharge length increases rapidly between steps (100 W and 200 W). The trends in the discharge length are then only considered for the range of 200 W to 600 W where the discharge length increases smoothly. The

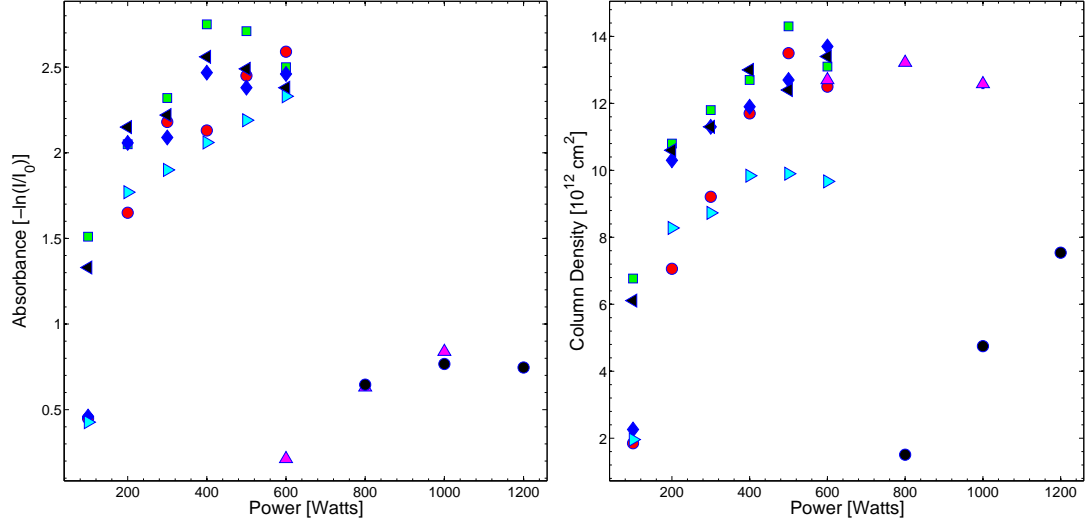


Figure 25. The absorbance of the s5 metastable state, left, shows a distinct trend, as power increases the absorbance increases. When a line-width adjusted cross-section is used to calculate the column density, right, the trend becomes less distinct but is still apparent. The argon mixtures are represented by the different markers as follows: 2% argon - \circ , 3% argon - \square , 4% argon - \diamond , 5% argon - ∇ , 10% argon - \star , 25% argon - \star

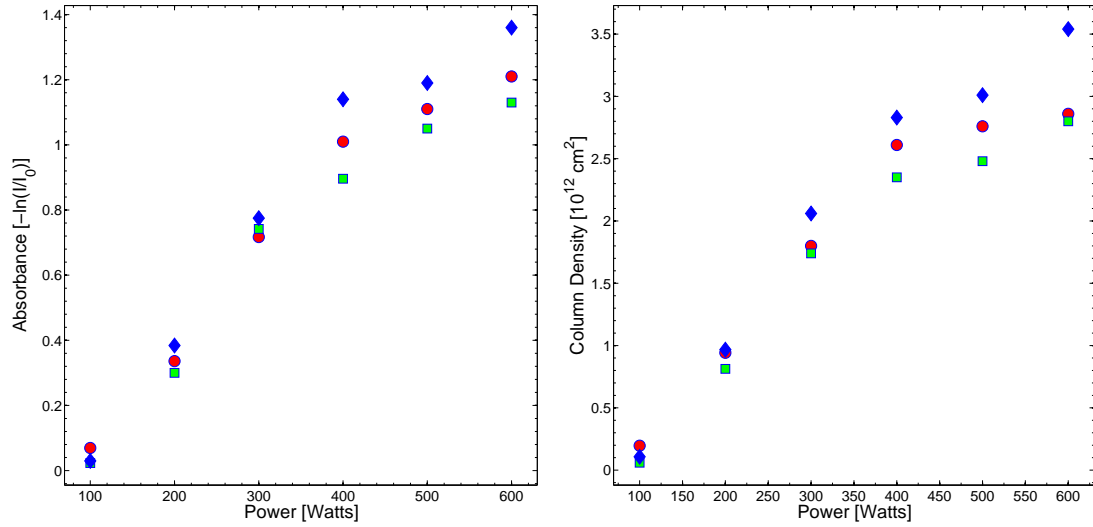


Figure 26. The absorbance of the s3 metastable state, left, shows a distinct trend, as power increases the absorbance increases. When a line-width adjusted cross-section is used to calculate the column density, right, the trend becomes less distinct but is still apparent. The argon mixtures are represented by the different markers as follows: 2% argon - \circ , 3% argon - \square , 4% argon - \diamond

number density, considering this small increase in discharge length, is increasing as the RF power is increased.

The final point of interest in the absorbance and column density data is in the high-pressure, high-power points found in Figure 25. As the RF power increases from 600 - 800 Watts for the 200 Torr case and from 800 - 1500 Watts in the 300 Torr case there is a rise in the absorbance. This trend looks favorable for producing a large enough metastable density at higher powers. Unfortunately, while the trend appears favorable the actual values of the column density and the corresponding number density are very low. These low metastable densities are likely the reason for an absence of laser performance early in the tests.

VI. Conclusions and Future Work

Capacitively-coupled and inductively-coupled radio-frequency discharges were shown to be maintainable and relatively stable at high pressures, around 300 Torr, and high RF powers, about 1 kW. OES and TDLAS were used to examine the metastable population and p-state population distributions as a function of the discharge parameters: total gas pressure, argon percent in gas, RF power and discharge type. OES measurements made a study of the p-state population distribution in many different discharge configurations possible. The p-state populations appear to approach a local equilibrium as the pressure in the discharges is increased. Furthermore, the populations become less statistical as the RF power is increased. The comparison of line intensities and the comparison of these p-state populations revealed that the argon pen lamp and microwave spectra excite a similar p-state distribution and that the CC discharge differs only in a higher production rate for the higher lying p-states. The inductively coupled discharge produces an order of magnitude more population in all the excited states. The significant affect of helium on the IC and CC discharge was shown by a comparison of the argon-helium population distributions to the pure argon population distributions in Zhu et. al (26). The s5 and s3 metastable column densities were found to decrease with increasing pressure and to increase with increasing RF power but a roll-over is present in the power curve leading to the belief that increases in power are not a viable compensation for loss in metastable column density due to increases in gas pressure. These column densities likely have their respective trends due to the change in the discharge exciation length implying a smaller decrease in the number densities when compared to the column densities with increasing pressure. Approximate Voigt fits to the absorbance data give Lorentzian and Doppler widths for the absorption profiles. From the Lorentzian widths an estimate of 18 ± 5.8 MHz/Torr was derived for the pressure broadening rate for the 801.48

nm $p8 \rightarrow s5$ transition and a rate of 22 ± 1.2 MHz/Torr for the 794.82 nm $p4 \rightarrow s3$ transition. The Doppler width showed scattered behavior but was used to calculate an approximate temperature range for the gas of 1300 - 2200 K for the IC discharge between 10 and 300 Torr and RF powers ranging from 0.1 to 1.5 kW. Large errors arise from the low fidelity of the data and the method by which the fits were conducted. These large errors correspond to the large range of pressure broadening rates for the $s5$ transition as well as the wide range of potential gas temperatures extracted from the Doppler width. A fitting routine that took into account the temperature dependence of the Lorentzian width with improved data will allow for extraction of a more accurate pressure broadening rate and an accurate gas temperature.

6.1 Future Work

Comparison of CC and IC metastable density trends

In order to effectively decide which discharge configuration is optimal a metastable absorption comparison test must be done. This will include measuring absorption for the $s3$ and $s5$ metastable levels in a CC discharge at the same pressures previously done for an IC discharge. The powers for the CC case are expected to be significantly lower with the hopes that similar powers to the IC case will produce considerably more metastable population. Once this comparison is done and the trends are compared, the decision can be made to tackle the heat loading problem associated with a specific configuration. Ideally, the study is expanded to consider different types of discharges. An expansive absorption study would include dielectric barrier discharges, micro-discharge arrays and high voltage narrow gap discharges for which both the metastable concentration and p-state population distribution could be examined. This extensive study would provide the evidence required to decide which discharge configuration is optimal for development of a low discharge power

CW DANGL. Future work should also examine the influence of the AC frequency on the production and destruction of metastables to find the optimal frequency for operation. This would be a fairly straightforward test, potentially using the same variable frequency RF equipment that was used in the high power experiments discussed. High metastable populations are developed in DC pulsed (1 kHz) discharge configurations and so there is an expectation of a large variation in the excited state distribution based on the discharge frequency (11).

Discharge Engineering Design

As mentioned in Chapter 4 there is much area for improvement in the design of the CC and IC discharges. A smaller I.D. should allow for improved high pressure performance and scaling up to higher pressures if deemed necessary. A better cooling system is required in order to function at high pressures due to the higher powers necessary to maintain the discharges. The discharge cell must be cooled using at best, a water jacket and at minimum, a high-pressure air flow. In order to improve laser performance the metastables should also be pumped downstream of the discharge. This is as simple as adding a cross to the flow downstream of the discharge with Brewster angle windows and constructing the laser resonator at that location. This design would allow pumping perpendicular to the flow of the gas.

If high power discharges cannot produce the necessary amount of metastables then the simple, single cell RF discharge idea must be changed. One possibility is in dielectric barrier discharges where, in the simplest sense, a parallel-plate or cylindrical capacitor partially filled with a dielectric is run at high voltage. In this case the high-pressure argon-helium gas would flow through a small-gap discharge (on the order of millimeters) and then expand upstream of the discharge where it can be pumped by the laser. These narrow gap discharges are commercially available

making this method a fairly straightforward approach. Another approach would be a high-power multi-cell configuration where multiple medium-pressure, medium-power cells, which together provide the necessary pressure and metastable concentration, are used together. These cells flow together and are then pumped downstream of the discharges. The problems with such an arrangement is due to the easy deactivation of the metastables. The multiple cells would have to flow into a large pipe which would then have to narrow slowly to achieve the required pressure. Any sharp turns will be bad for the system as metastable deactivation through collisions with these edges is likely.

Discharge and Gas Kinetic Model

The kinetics of the argon helium gas discharge are complicated. Incomplete sets of hundreds of kinetic mechanisms and rates for argon-electron and argon-argon collisions can be found in the Zhu et. al paper (26) and helium-electron and helium-helium collisions can be found in Fujimoto paper (7). These rate packages tend to cover many different regimes in the discharge from the low-pressure regime, dominated by electron excitation and optical de-excitation, to the high-pressure regime dominated by gas collisions that cause mixing between the levels. In general these rates are functions of the electron density, electron temperature, and the gas temperature. This represents the need for a kinetic model that describes not only the gas kinetics but also the power loading and energy transfer kinetics from the discharge to the gas as well as the model of discharge behavior, which has spatial variation. Presently, no such model exists. The development of such a predictive model would be an important asset in assessing discharge conditions and how they impact the metastable concentration in order to optimize the discharges for a laser system. In order to develop such a model the gas kinetics would have to be expanded to include the argon-helium collisions and

not just the relatively well known argon-argon, argon-electron, helium-electron and helium-helium collisions. A first step would be to use the hard-sphere approximation with a Boltzmann energy offset to approximate the argon helium mixing kinetics (3). The introduction of a power loading model that relates the input RF power, the absorbed power, electron density and electron temperature would also be necessary. There are many codes that, provided a rate package, can do just that. An example of one of those codes is Bolsig, which solves the Boltzmann equation for different gases given the conditions of gas composition and the E/N ratio (10). Another code that is an expansion of Bolsig+ is ZDPlasKin, a zero-dimensional plasma kinetic model. ZDPlasKin is essentially a wrapper for Bolsig+ and solving the Boltzmann equation using an input of chemical reactions and rates as well as the plasma conditions (16).

Appendix A. Grotrian Diagram

An energy level diagram that only includes the s and p states is shown in Figure 27.

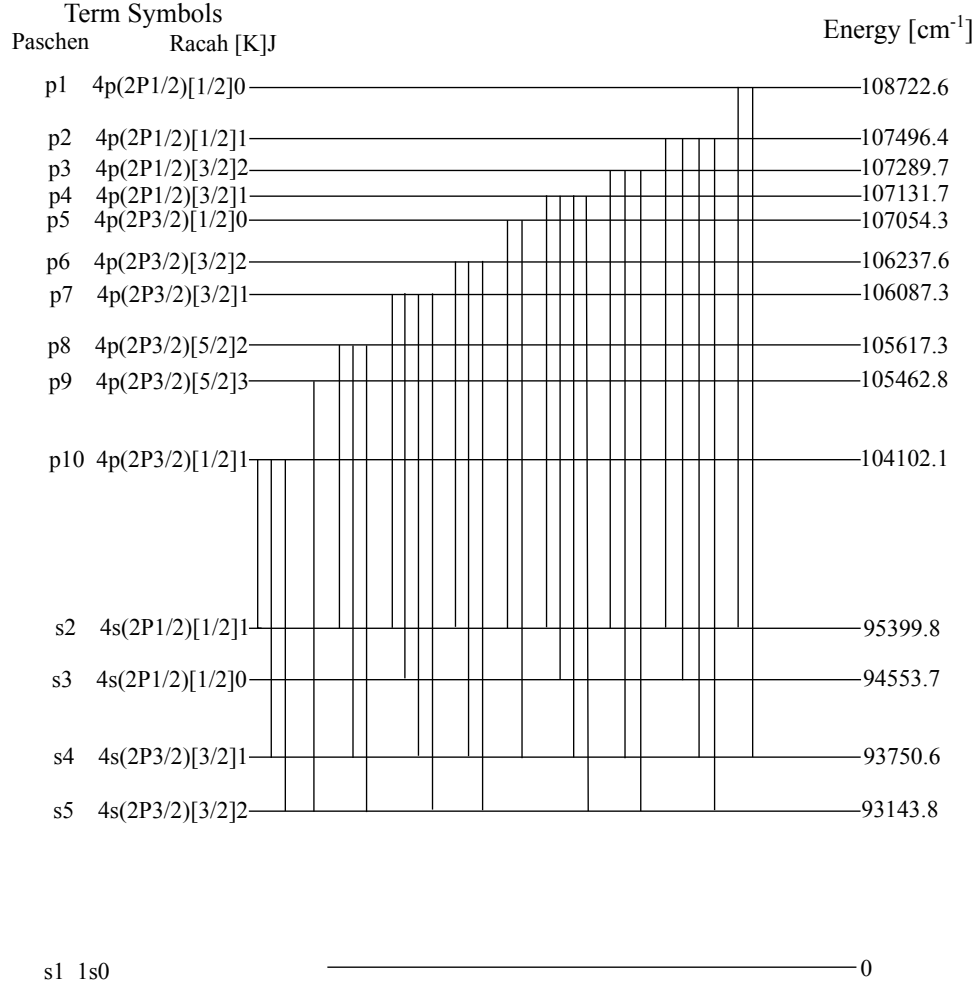


Figure 27. The energy level diagram for excited argon is shown focusing only on the s and p excited levels. The levels are denoted both by their Paschen and Racah designations on the left as well as their distance from ground on the right.

Appendix B. Matching Network

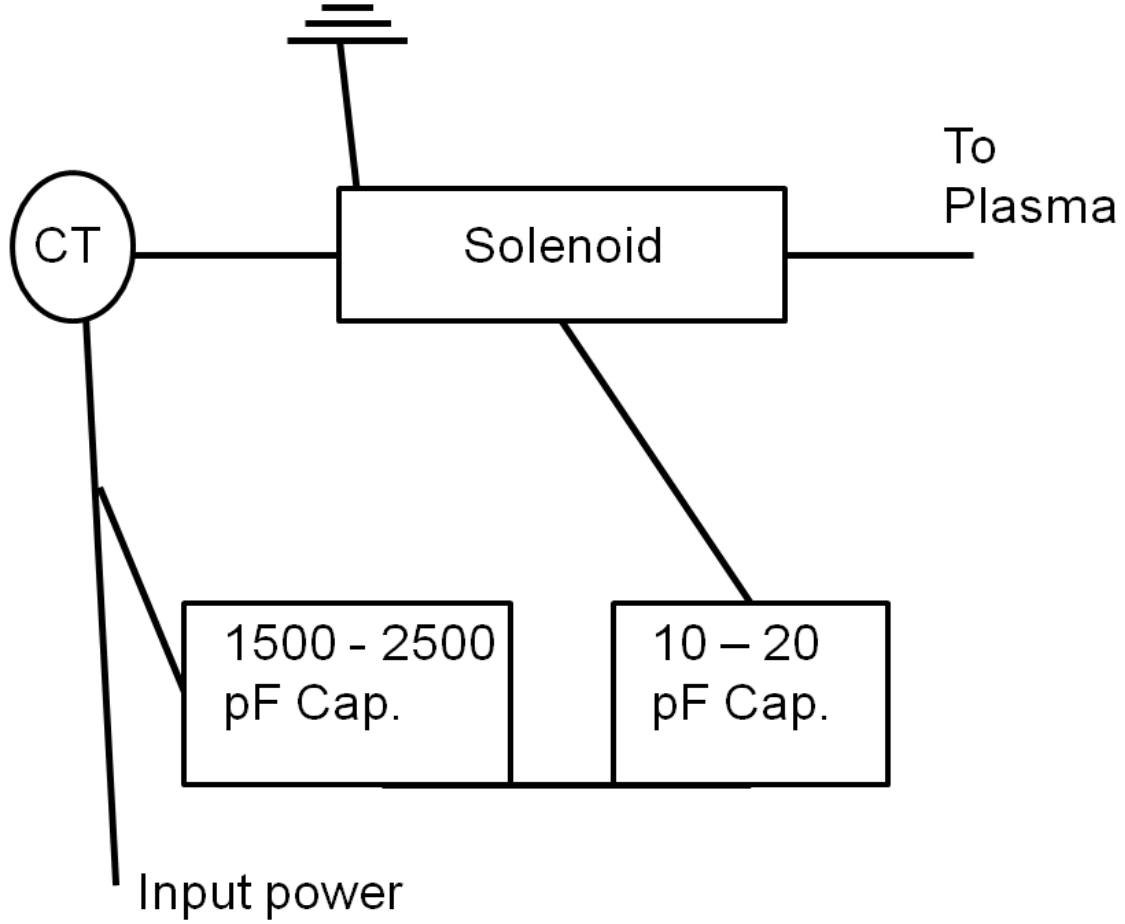


Figure 28. The diagram of the modified pi matching network used in these experiments. The input power goes through a current transformer to allow for current measurement. The current then runs through a solenoid which is designed to be a good resistance and impedance match to the plasma load. Connected in parallel to the set up are two capacitors with tunable capacitances. The current leaves the solenoid and runs to the discharge.

The matching network depicted in Figure 28 is a variation of the Pi matching network. The matching network has a load specific design which is important in allowing the network to properly impedance match. The impedance of any circuit element is given by:

$$Z = R + iX \quad (24)$$

where Z is the impedance, R is the resistance and X is the reactance. The solenoid is designed to match the resistance of the expected load including the wires. In general, this is done by filling a reference cell with an atmosphere of gas and testing the resistance on the discharge. The solenoid is also designed to match the impedance of the system load. Since exact matching of these values is dependent on the exact plasma conditions some tuning ability is required. If the solenoid in the matching network is properly resistance matched then this impedance matching can be done purely for the imaginary part of the impedance, or the reactance. The reactance is given by:

$$X = \omega L - \frac{1}{\omega C} \quad (25)$$

where ω is the AC frequency. The reactance matching is done by adding two tunable capacitors, of different capacitance ranges, in parallel to the solenoid. By tuning these capacitors the reactance can be properly matched. The large difference in the capacitances seen in Figure 28 allows for a fine and coarse tuning. Since the reactance has a $\frac{1}{C}$ dependence the smaller capacitance capacitor acts as a coarse tune since it will impact the total reactance in a much more significant way. The large capacitance will then be the fine tune to allow for a more precise matching of the reactances.

Appendix C. IC and CC Spectra

The influence of RF power on the overall intensity and the relative intensity of certain lines is examined. Spectra of the CC discharge are shown in Figure 29 as the RF power varies from 100 Watts, top, to 200 Watts, middle, to 300 Watts, bottom. The overall intensity of the lines increase but this increase in intensity is not uniform and changes the comparative height of closely spaced lines. This is most clearly seen in the 810.37 nm and 811.53 nm pair for which the former increases more rapidly than the latter. This is consistent with a more rapidly increasing population in the upper states as the 810.37 line originates on the p7 upper state whereas the 811.53 nm line originates on the p9 upper state. Similarly, the relative intensity of the 750.39 nm and 751.47 nm pair changes. As stated, the higher lying states are being populated more rapidly with increases in power and so, as expected, the 750.39 nm line which originates on the p1 state intensifies faster than the 751.47 nm line which originates on the p5 state.

Worth noting is the increasing intensity of the 844 nm and barely visible 777 nm atomic oxygen triplets. As the power increases more of the oxygen in the welding grade argon is dissociated and excited. The IC discharge in Figure 30 has a drastically different spectrum compared to the CC discharge.

The intensity of the spectral lines in the IC discharge do not increase dramatically as the RF power increases from 600 to 800 Watts. The atomic nitrogen lines about 819 nm increase as the RF power increases.

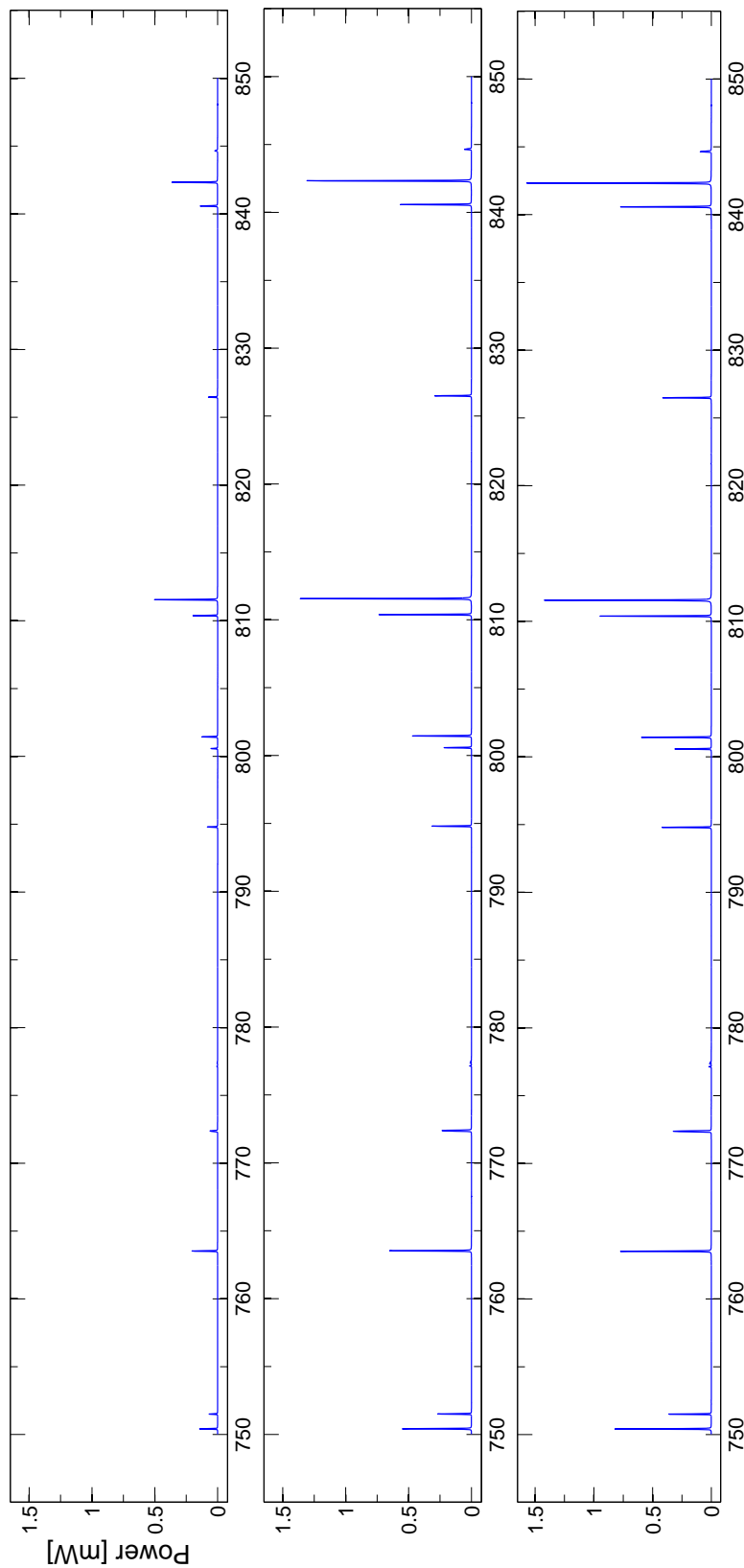


Figure 29. The spectral shown are for a CC discharge with a 5% argon mixture at 100 Torr with RF power increasing from 100 Watts, top, to 200 Watts, middle, to 300 Watts, bottom. Intensity of the observed spectral lines increases as the RF power of the CC discharge increases. Intensity of lines originating on higher energy upper states, 750.39 nm and 810.37 nm, increase more rapidly with power when compared to nearby spectral lines.

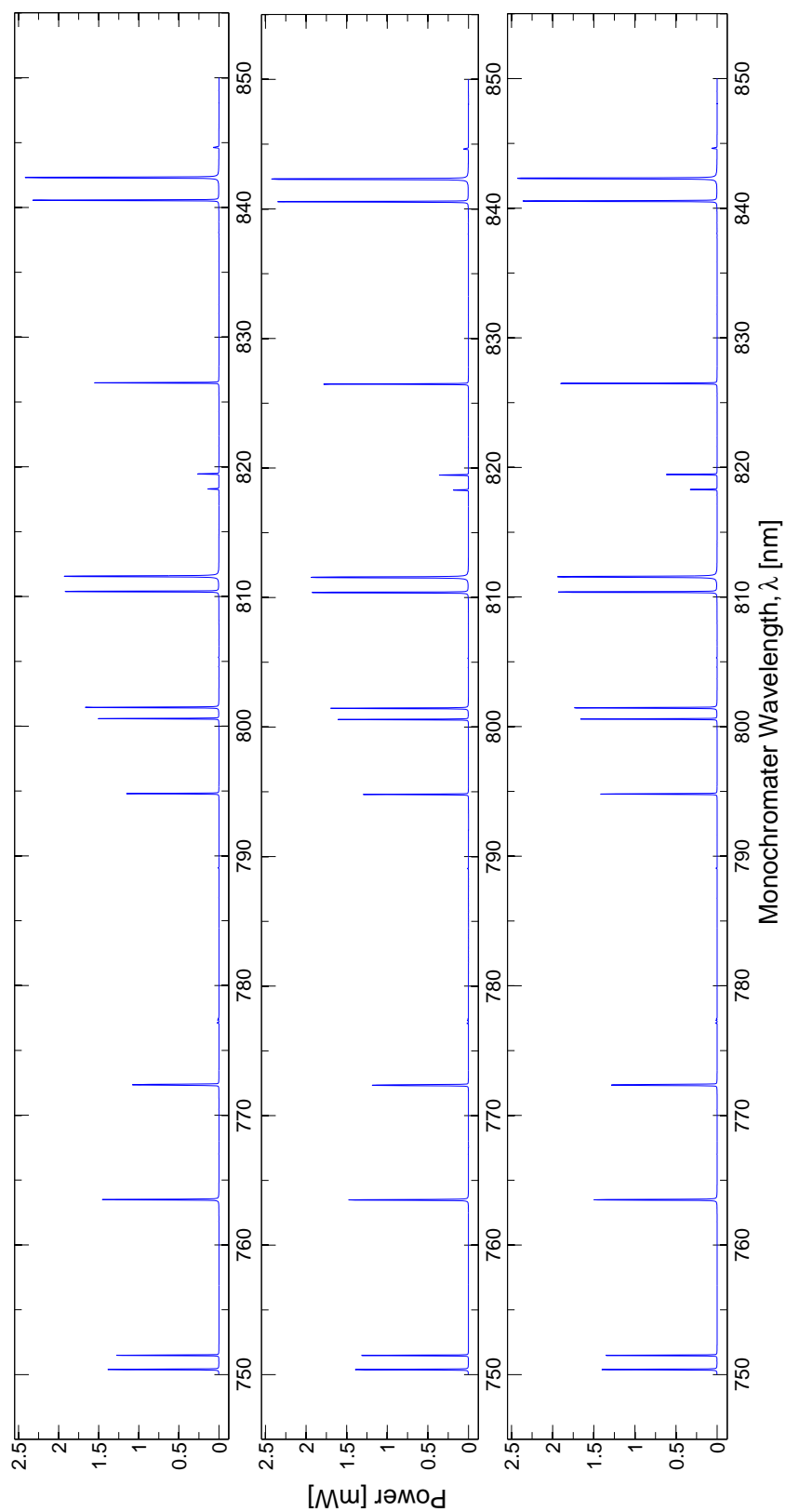


Figure 30. The spectral shown are for a IC discharge with a 5% argon mixture at 100 Torr with RF power increasing from 600 Watts, top, to 800 Watts, middle, to 800 Watts, bottom. Intensity of the observed spectral lines appears to change little as the RF power increases. The atomic Nitrogen lines about 819 nm increase as the RF power increases.

Appendix D. Population Distributions

The population distributions for the spectra shown in Appendix C are compared in Figure 31 and Figure 32. The squares in these figures represent populations calculated from transitions that terminate on the metastable states and the diamonds for those that terminate on resonance states. The population distribution for the CC discharge at 100 Torr, 100 Watts, left, and 300 Watts, right, are marked with their appropriate p-state labels. As before, we see that the p7 spacing between the resonance and metastable states is flipped compared to that of the p6, p4, p3 and p2 states. There is clear evidence, however, for radiation trapping as the spacing between the metastable and resonance populations calculated from those spectral lines increases as the power increases.

The populations distributions for the IC discharge at 100 Torr, 600 Watts, left, and 800 Watts, right, are shown. The populations of the excited p-states increase slightly between the left plot, at 600 Watts, and the right plot, at 800 Watts. The peaks of the aforementioned pairs are all about equal despite the shift to higher populations. This small increase in population points to the excitation of higher lying states. If the production and destruction of the p-states has reached a kinetic steady state that is independent of the RF power then we would expect this trend to occur. Additional RF power may be exciting states above the p-states and so not dramatically changing the intensities of the lines originating on p-states.

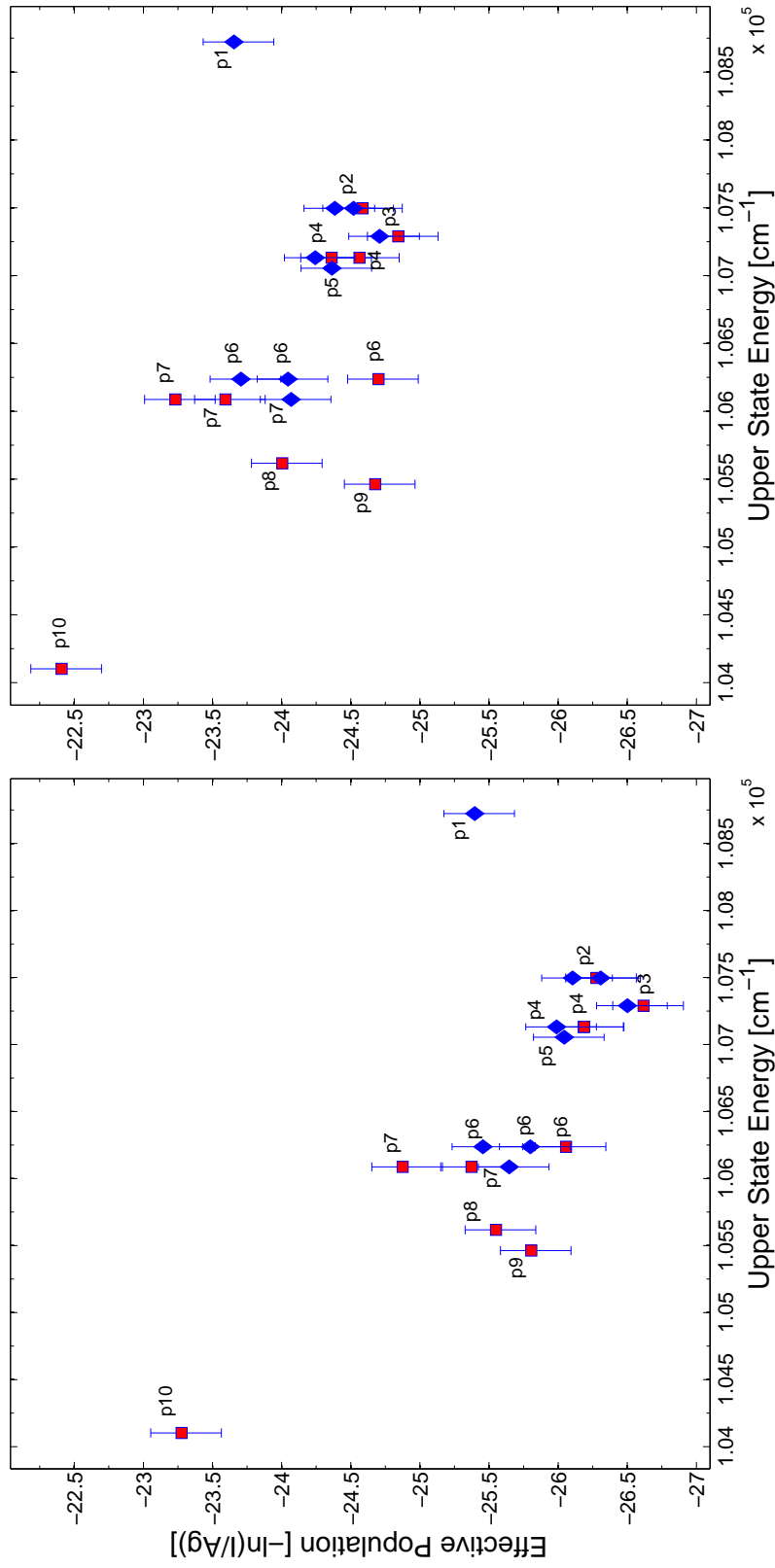


Figure 31. The calculated populations change for a CC discharge with 5% argon at 100 Torr and 100 Watts, left, to 300 Watts, right. The p7 transitions terminating on metastable states report a higher population relative to the resonance terminated transition. The spacing between the p6, p4, p3 and p2 metastable terminated transitions and the resonance terminated transitions increases with RF power providing evidence for radiation trapping in the discharge.

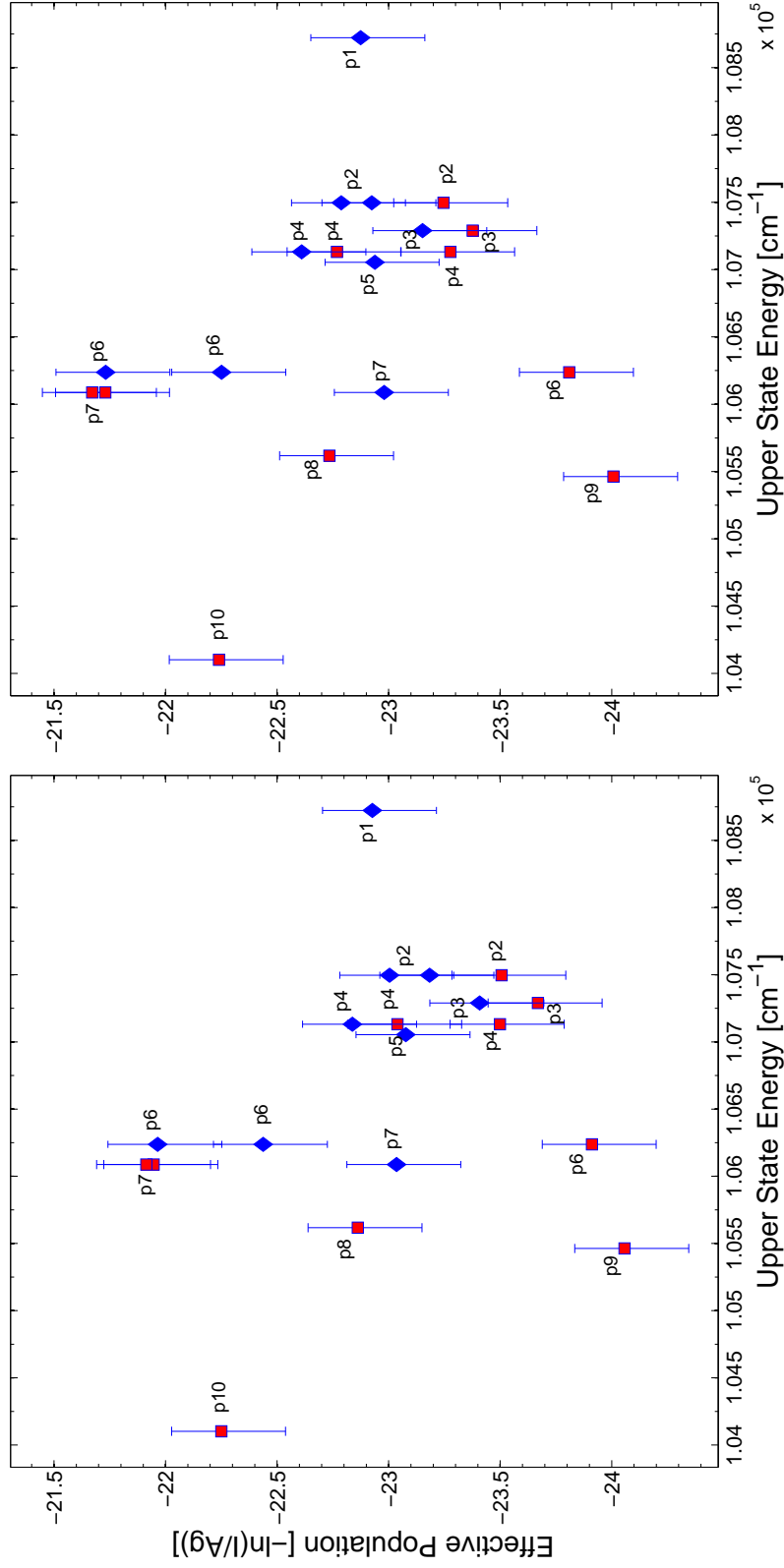


Figure 32. The calculated populations do not change significantly for a IC discharge with 5% argon at 100 Torr and 600 Watts, left, to 800 Watts, right. The p7 transitions terminating on metastable states report a higher population relative to the resonance terminated transition. There is a large spacing between the p6 metastable terminated transition and resonance terminated transition as well as a medium spacing between the p4, p3 and p2 transitions. This provides evidence for a large amount of radiation trapping in the cells.

Bibliography

1. Balcon, N. et al. “Numerical Model of an Argon Atmospheric Pressure RF Discharge”. *IEEE Transactions on Plasma Science*, 36(5):2782–2787, 2008.
2. Belostotskiy, Sergey G. et al. “Spatially resolved measurements of argon metastable ($1s_5$) density in a high pressure microdischarge using diode laser absorption spectroscopy”. *IEEE Transactions on Plasma Science*, 37(6):852–858, 2009.
3. Berry, R. Stephen et al. *Physical and Chemical Kinetics*. Oxford University Press, New York, New York, 2002.
4. Binder, Raymond C. *Fluid Mechanics*. Prentice-Hall Inc., Englewood Cliffs, NJ, 1973.
5. Boffard, John B. et al. “Measurement of metastable and resonance level densities in rare-gas plasmas by optical emission spectroscopy”. *Plasma Sources Sci. Technol.*, 18(3), 2009.
6. Bogachev, A.V. et al. “Diode-pumped caesium vapour laser with closed-cycle laser-active medium circulation”. *Quantum Electronics*, 42(95):95–98, 2012.
7. Fujimoto, Takashi. “A Collisional Radiative Model for Helium and Its Applications to a Discharge Plasma”. *Journal of Quantitative Spectroscopy and Radiative Transfer*, 21:439–455, 1979.
8. Gangwar, R. K. et al. “Argon plasma modeling with detailed fine-structure cross sections”. *Journal of Applied Physics*, 111:053307–1 – 053307–9, 2012.
9. Giulio, Racah. “Theory of Complex Spectra. I”. *Physical Review*, 61:186–197, 1942.
10. G.J.M., Hagelaar and L.C. Pitchford. “Solving the Boltzmann equation to obtain electron transport coefficients and rate coefficients for fluid models”. *Plasma Sources Sci. Technol.*, 14:722–733, 2005.
11. Han, Jiande and Michael C. Heaven. “Gain and lasing of optically pumped metastable rare gas atoms”. *Optics Letters*, 37(11):2157–2159, 2012.
12. Iordanova, S. and I. Koleva. “Optical emission spectroscopy diagnostics of inductively-driven plasmas in argon gas at low pressures”. *Spectrochimica Acta Part B*, 62:344–356, 2007.
13. Krupke, William F. “Diode pumped alkali lasers (DPALs): an overview”. *SPIE*, 7005, 2008.

14. Li, Jiang et al. "The population distribution of argon atoms in Paschen 1s levels in an inductively coupled plasma". *Journal of Physics D: Applied Physics*, 43:1–11, 2010.
15. Morajev, M. et al. "Physics of high-pressure helium and argon radio-frequency plasmas". *Journal of Applied Physics*, 96(12):7011–7017, 2004.
16. Pancheshnyi, S. et al. "Computer code ZDPlasKin". 2008. [Http://www.zdplaskin.laplace.univ-tlse.fr](http://www.zdplaskin.laplace.univ-tlse.fr) (University of Toulouse, LAPLACE, CNRS-UPS-INP, Toulouse, France).
17. Park, Jaeyoung. et al. "Discharge phenomena of an atmospheric pressure radio-frequency capacitive plasma source". *Journal of Applied Physics*, 89(1):20–28, 2004.
18. Perram, Glen. P. et al. *Introduction to Laser Weapon Systems*. Directed Energy Professional Society, Albuquerque, NM, 2010.
19. Sadeghi, N. and D.W. Setser. "Quenching rate constants for reactions of $\text{Ar}(4p'[1/2]_0, 4p[1/2]_0, 4p[3/2]_2, \text{ and } 4p[5/2]_2)$ atoms with 22 reagent gases". *Journal of Chemical Physics*, 115(7):3144–3154, 2001.
20. Scheller, Geoffrey. R. et al. "Quenching rates of Ar metastables in radiofrequency glow discharges". *Journal of Applied Physics*, 64(2):598–606, 1988.
21. Thompson, William J. "Numerous neat algorithms for the Voigt profile function". *Computers in Physics*, 7(6):627–631, 1993.
22. Vasile, M. J. "A comparative study of the radio-frequency discharge in gas mixtures of helium with fluorine, oxygen, nitrogen and argon". *Journal of Applied Physics*, 51(5):2503–2509, 1980.
23. Velazco, J.E. et al. "Rate constants and quenching mechanisms for the metastable states of argon, krypton and xenon". *Journal of Chemical Physics*, 69(10):4357–4373, 1978.
24. Verdeyen, Joseph T. *Laser Electronics*. Prentice-Hall Inc., Englewood Cliffs, New Jersey, 1995.
25. Wiese, W.L. et al. "Atomic transition probabilities, Vol. II: Sodium through calcium - A critical data compilation". NSRDS-NBS 22:268, 1969.
26. Zhu, Xi-Ming et al. "A simple collisional-radiative model for low-temperature argon discharges with pressure ranging from 1 Pa to atmospheric pressure: kinetics of Paschen 1s and 2p levels". *Journal of Physics D: Applied Physics*, 43:1–17, 2009.

Vita

Mr. Ben Eshel was born and raised in Saddle Brook, NJ. He attended the Telecommunications and Computer Science Academy of Bergen County Academies in Hackensack, NJ. He then attended Cornell University where he recieved a B.A. in Physics. After graduation he applied and was accepted to the Air Force Institute of Technology for an M.S. in Applied Physics. After recieving his M.S. Mr. Eshel plans to continue his studies with the hopes of recieving a PhD in Applied Physics, also from The Air Force Institute of Technology.

REPORT DOCUMENTATION PAGE

Form Approved
OMB No. 0704-0188

The public reporting burden for this collection of information is estimated to average 1 hour per response, including the time for reviewing instructions, searching existing data sources, gathering and maintaining the data needed, and completing and reviewing the collection of information. Send comments regarding this burden estimate or any other aspect of this collection of information, including suggestions for reducing this burden to Department of Defense, Washington Headquarters Services, Directorate for Information Operations and Reports (0704-0188), 1215 Jefferson Davis Highway, Suite 1204, Arlington, VA 22202-4302. Respondents should be aware that notwithstanding any other provision of law, no person shall be subject to any penalty for failing to comply with a collection of information if it does not display a currently valid OMB control number. **PLEASE DO NOT RETURN YOUR FORM TO THE ABOVE ADDRESS.**

1. REPORT DATE (DD-MM-YYYY) 13-06-2013		2. REPORT TYPE Master's Thesis		3. DATES COVERED (From — To) August 2011 — June 2013	
4. TITLE AND SUBTITLE Spectral analysis and metastable absorption measurements of high pressure capacitively and inductively coupled radio-frequency argon helium discharges				5a. CONTRACT NUMBER	
				5b. GRANT NUMBER	
				5c. PROGRAM ELEMENT NUMBER	
6. AUTHOR(S) Eshel, Ben				5d. PROJECT NUMBER	
				5e. TASK NUMBER	
				5f. WORK UNIT NUMBER	
7. PERFORMING ORGANIZATION NAME(S) AND ADDRESS(ES) Air Force Institute of Technology Graduate School of Engineering and Management (AFIT/EN) 2950 Hobson Way WPAFB OH 45433-7765				8. PERFORMING ORGANIZATION REPORT NUMBER AFIT-ENP-13-J-02	
9. SPONSORING / MONITORING AGENCY NAME(S) AND ADDRESS(ES) High Energy Laser Joint Technology Office 801 University Blvd. SE, Suite 209 Albuquerque, NM 87106 Phone: 505-248-8208 Email: harro.ackermann@jto.hpc.mil				10. SPONSOR/MONITOR'S ACRONYM(S) HEL JTO	
				11. SPONSOR/MONITOR'S REPORT NUMBER(S)	
12. DISTRIBUTION / AVAILABILITY STATEMENT APPROVED FOR PUBLIC RELEASE; DISTRIBUTION UNLIMITED.					
13. SUPPLEMENTARY NOTES					
14. ABSTRACT Characterization of the excited state argon population in an argon-helium discharge is of crucial importance to the development of a continuous wave Discharge Assisted Noble Gas Laser. Experiments were conducted in the Richard W. Davis Advanced Laser Facility at AFRL on Kirtland Air Force Base, Albuquerque, NM. During these tests the capability to maintain a capacitively-coupled and inductively-coupled radio-frequency discharge at pressures of 300 Torr was demonstrated. Optical Emission Spectroscopy experiments were conducted in order to examine the population distribution of the p-state in argon. The population distributions for these high-pressure and high-power cases were compared to a low-pressure, low-power pure argon discharge to examine the influence of helium on an argon discharge. Tuneable Diode Laser Absorption Spectroscopy experiments were also performed on the inductively coupled discharge to examine the column density of the s5 and s3 metastable states for different discharge parameters. The absorption data was fit to an approximated Voigt profile from which pressure broadening rates of 18 ± 5.8 MHz/Torr and 22 ± 1.2 MHz/Torr were calculated for the 801.48 nm p8 → s5 and 794.82 nm p4 → s3 transitions, respectively.					
15. SUBJECT TERMS high-pressure discharge, argon kinetics, DANGL, metastable density					
16. SECURITY CLASSIFICATION OF:			17. LIMITATION OF ABSTRACT	18. NUMBER OF PAGES	19a. NAME OF RESPONSIBLE PERSON
a. REPORT	b. ABSTRACT	c. THIS PAGE			Dr. Glen P. Perram, AFIT/ENP
U	U	U	U	86	19b. TELEPHONE NUMBER (include area code) (937) 255-3636, x4504; Glen.Perram@afit.edu